

Ames Contrail Simulation Model: Modeling Aviation Induced Contrails and the Computation of Contrail Radiative Forcing Using Air Traffic Data

Jinhua Li

NASA Langley Research Center, Hampton, Virginia

Jung-Hong Kim

Seoul National University, Seoul, Republic of South Korea

Banavar Sridhar

Universities Space Research Associate, Moffett Field

Hok K. Ng

NASA Ames Research Center, Moffett Field, California

NASA STI Program Report Series

Since its founding, NASA has been dedicated to the advancement of aeronautics and space science. The NASA scientific and technical information (STI) program plays a key part in helping NASA maintain this important role.

The NASA STI program operates under the auspices of the Agency Chief Information Officer. It collects, organizes, provides for archiving, and disseminates NASA's STI. The NASA STI program provides access to the NTRS Registered and its public interface, the NASA Technical Reports Server, thus providing one of the largest collections of aeronautical and space science STI in the world. Results are published in both non-NASA channels and by NASA in the NASA STI Report Series, which includes the following report types:

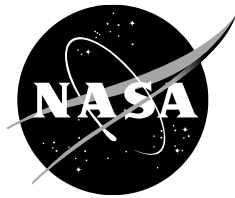
- **TECHNICAL PUBLICATION.** Reports of completed research or a major significant phase of research that present the results of NASA Programs and include extensive data or theoretical analysis. Includes compilations of significant scientific and technical data and information deemed to be of continuing reference value. NASA counterpart of peer-reviewed formal professional papers but has less stringent limitations on manuscript length and extent of graphic presentations.
- **TECHNICAL MEMORANDUM.** Scientific and technical findings that are preliminary or of specialized interest, e.g., quick release reports, working papers, and bibliographies that contain minimal annotation. Does not contain extensive analysis.
- **CONTRACTOR REPORT.** Scientific and technical findings by NASA-sponsored contractors and grantees.

- **CONFERENCE PUBLICATION.** Collected papers from scientific and technical conferences, symposia, seminars, or other meetings sponsored or co-sponsored by NASA.
- **SPECIAL PUBLICATION.** Scientific, technical, or historical information from NASA programs, projects, and missions, often concerned with subjects having substantial public interest.
- **TECHNICAL TRANSLATION.** English-language translations of foreign scientific and technical material pertinent to NASA's mission.

Specialized services also include organizing and publishing research results, distributing specialized research announcements and feeds, providing information desk and personal search support, and enabling data exchange services.

For more information about the NASA STI program, see the following:

- Access the NASA STI program home page at <http://www.sti.nasa.gov>
-



Ames Contrail Simulation Model: Modeling Aviation Induced Contrails and the Computation of Contrail Radiative Forcing Using Air Traffic Data

Jinhua Li

NASA Langley Research Center, Hampton, Virginia

Jung-Hong Kim

Seoul National University, Seoul, Republic of South Korea

Banavar Sridhar

Universities Space Research Association, Moffett Field, California

Hok K. Ng

NASA Ames Research Center, Moffett Field, California

National Aeronautics and
Space Administration

Langley Research Center
Hampton, Virginia 23681-2199

December 2023

The use of trademarks or names of manufacturers in this report is for accurate reporting and does not constitute an official endorsement, either expressed or implied, of such products or manufacturers by the National Aeronautics and Space Administration.

Available from:

NASA STI Program / Mail Stop 050
NASA Langley Research Center
Hampton, VA 23681-2199

Acknowledgments

The authors wish to acknowledge the help of Ulrich Schumann at DLR in the development of the radiative forcing contrail computations and questions relating to CoCiP software.

Some of the components of the ACSM were developed by Fabio Caizzo during his summer internship at the NASA Ames Research Center.

We also want to thank Dr. William Smith at the NASA Langley Research Center for his insightful comments on this report.

Abstract

NASA is developing traffic flow management strategies to reduce the impact of aviation on climate and improve efficiency of aircraft routes in the presence of limited airport and airspace capacity constraints, which are partly due to convective weather and natural calamities. Development of Strategic Traffic Flow Management (STFM) requires models of aircraft emissions and contrails, and models of their effect on climate. There is extensive literature on the modeling of contrails and the Radiative Forcing (RF) associated with contrails. This report captures the latest NASA developments in this research area and describes the integrated modeling, analysis, and software development to support STFM. Aircraft contrails are long, thin and often linear clouds triggered by aircraft engine exhausts in the high-altitude ice-saturated atmosphere. Contrails, similar to that of natural cirrus clouds, can impact global climate by reflecting shortwave radiation and trapping longwave radiation. Recent studies from the Intergovernmental Panel on Climate Change (IPCC) have shown that aircraft contrails are estimated to have greater impact on global warming than aircraft CO_2 emissions. The Ames Contrail Simulation Model (ACSM) presented in this report simulates the full life cycle of aircraft contrails, including their formation, dynamic evolution, and dissipation, and calculates the associated RF with actual meteorological and air traffic data. ACSM combines models from previous studies that focus on contrail formation and persistence based on the Schmidt-Appleman theoretical criteria, and it incorporates elements of cloud dynamics, microphysics, and climate modeling found in other surveyed contrail models, while also making adjustment for improved computational efficiency. In addition, ACSM is integrated with NASA's state-of-the-art flight simulation software for rapid assessment of aircraft contrail impacts. Applications include assessments of long-term global climate impact resulting from aviation-induced contrails and the design of optimal contrail-mitigation aircraft operation strategies.

Table of Contents

1. Introduction	6
2. Life Cycle of Contrails	8
2.1 Stanford's Aircraft Contrail Model	8
2.2 Burkhardt-DLR Aircraft Contrail Model	9
2.3 CoCiP-DLR Aircraft Contrail Model	9
3. Ames Contrail Simulation Model	11
3.1 Contrail Formation	11
3.2 Contrail Persistence and Age	15
3.3 Wake Vortex Turbulence Model	16
3.4 Contrail Initial Shape and Concentration	16
3.5 Advection Model	18
3.6 Diffusion Model	20
3.7 Contrail Cloud Microphysics Model	21
4. Contrail RF	26
4.1 CoCiP RF model	27
5. Radiative forcing calibration of ACSM	30
6. Case study with one-day of US air traffic	36
7. Conclusion	38
References	39
Appendixes	42
Appendix A. Terminologies	42
Appendix B. Contrail radiative forcing parameter table	43
Appendix C. Instruction to download MERRA data	44
Appendix D. Instruction on source codes	45

Figure 1. ACSM model structure	8
Figure 2. Burkhardt-DLR's aircraft contrail model structure (dotted boxes and arrows represent the additional modules and processes compared to ACSM).....	9
Figure 3. Relationship among contrail-formation meteorological parameters	13
Figure 4 Feasible ambient relative humidity w.r.t water for contrail forming.....	14
Figure 5. Appleman diagram from [12]	14
Figure 6. Ratio between relative humidity over ice and relative humidity over water	15
Figure 7. Contrail cross-section shapes: (a) rectangle with uniform concentration used in ACSM; (b) ellipse with uniform concentration used in Stanford's model; (c) ellipse with Gaussian distributed concentration used in CoCiP mode	16
Figure 8. Single ice particle terminal velocity over diameter using Eqn. (18)	19
Figure 9. Single ice particle terminal velocity over diameter using Eqn. (21): (top) $di \leq 100\mu m$; and (bottom) $di > 100\mu m$	20
Figure 10. Saturation ratio of water vapor w.r.t ice SV_i over temperature	23
Figure 11. Contrail ice particle diffusional growth: (top) normalized mass growth rate; (bottom) radius growth rate	24
Figure 12. Contrail ice particle radius growth by deposition at pressure 50kPa over time, which is consistent with results from CoCiP (Fig. 7 in [11])	25
Figure 13. Estimated aviation RF for 1992 and 2000 based on IPCC studies	26
Figure 14. Longwave (LW; blue line) and Shortwave (SW; red line) Radiative Forcing (RF) as a function of Solar Zenith Angle (SZA) for sphere habits, $\tau = 0.52$, $re_{eff} = 16\mu m$, $A = 0.2$, $S_0 = 1370W/m^2$, $T = -44.6oC$, and $OLR = 279.6W/m^2$	28
Figure 15. Net Radiative Forcing as a function of contrail optical depth (τ) at $0.55\mu m$ for various particle habits with $re_{eff} = 16\mu m$, $S_0 = 1370W/m^2$, $A = 0.2$, $SZA = 30o$, $OLR = 279.6W/m^2$, $T = -44.6oC$..	29
Figure 16. Global distributions of annual mean local (top) Shortwave (SW), (middle) Longwave (LW), and (bottom) net radiative forcing (RF) for globally homogeneous contrail layer with 1% cover at 10.5km altitude and particle properties from Myhre et al. [23]. From the top to bottom panels, area-weighted averages are -0.086(SW), 0.21(LW), and 0.13(net) W/m^2	31
Figure 17. Global horizontal distributions of the net radiative forcing from 1% homogeneous contrail cover at 10.5km altitude and particle properties from Myhre et al. [23] for 2013. Green boxes in US (20N-50N, 60W-130W) and North Atlantic Flight Corridor (NAFC)	32
Figure 18. Diurnal distributions of the potential climate impact due to the change of LW RF (green bars), SW RF (blue bars), and net RF (orange lines) by a 1% homogeneous contrail layer at 10.5km altitude in US (top) and North Atlantic Flight Corridor (NAFC) (bottom) regions. Note that the areas for these regions are depicted as green boxes in Fig. 17. Static value of $30mW/m^2$ is also depicted as red dash lines.	33
Figure 19. The same as Fig. 18 (top), Except for (a) Winter (December-February), (b) Spring (March-May), (c) Summer (June-August), and (d) Fall (September-November) in 2013.....	35
Figure 20. The same as Fig. 18 (bottom), except for (a) DJF, (b) MAM, (c) JJA, and (d) SON.	35
Figure 21. Horizontal distributions of the contrail-induced Radiative Forcing (RF; shading) in US at 00UTC (upper left), 06UTC (upper right), 12UTC (lower left), and 18UTC (lower right) on April 23, 2010.	36
Figure 22. Hourly distributions of the contrail-induced Radiative Forcing (RF; green bars) and averaged traffic density within a given $13km \times 13km$ grid box (orange line) in CONUS on April 23, 2010.....	37
Figure 23. Cloud water component microphysical processes	42

1. Introduction

Condensation trails, or *contrails*, are long, thin, and linear artificial clouds that form as a result of aircraft engine combustion in the ice-saturated upper troposphere (above 25,000ft or 8km). Contrails are caused by water vapor condensation and subsequent freezing on soot and aerosols in ice-saturated conditions in the upper troposphere at temperatures normally below -40°C . Contrails consist of water, in the form of a suspension of liquid droplets and ice particles. The lifespan of contrails varies from a few seconds to many hours before sublimation or dissipation depending on local atmospheric conditions. In this report, only contrails that persist for at least an hour are considered. During their lifetime, contrails can be transported hundreds of miles by winds and horizontal contrails can thinly spread over large areas of tens of square miles. Meanwhile, the microphysical properties of contrail clouds will change as the ice particles grow by the uptake of excessive water vapor contained in the surrounding atmosphere. Some linear contrails can also transform into contrail cirrus. Contrail cirrus is difficult, if not impossible, to distinguish visually from most natural cirrus. The microphysics and optical properties of contrail cirrus also resemble natural cirrus so that their Radiative Forcing (RF) can also be similar. It is commonly accepted that linear contrails and contrail cirrus resulting from global aviation activities have a net warming effect overall, as the effectiveness with which they trap outgoing longwave radiation (heating) exceeds the cooling effect caused by the reflection of solar short-wave radiation.

The main contributions of this work are around improving the scientific level of understanding for aviation-induced contrails and developing models which can be practically applied to minimize the negative impacts of aviation on climate. It is well accepted by international committees such as the Intergovernmental Panel on Climate Change (IPCC) that contrails resulting from aviation activities are one source of global warming along with carbon dioxide emission. However, the life cycle of aviation-induced contrails, from their formation to dissipation, consists of a series of complicated dynamic processes. Because of this complexity, the scientific level of understanding for aviation-induced contrails is labeled as poor by the IPCC experts. In comparison, the scientific level of understanding for carbon dioxide is labeled as good [1] [2] [3] [4]. To our knowledge, The Ames Contrail Simulation Model (ACSM) is among the very few models in the world that attempts to model the full life cycle of aviation-induced contrails and calculate the associated global warming effects estimated from radiative forcing calculations that utilize air traffic and meteorological data. The resulting contrail RF as a function of location and time can be used in designing aircraft routes that minimize the impact of aviation on climate.

The rest of the report is organized as follows.

- Section 2 describes the life cycle of aviation-induced contrails from their formation until dissipation and provides an overview of three state-of-the-art aviation contrail models developed at German Aerospace Center (DLR), and Stanford University.
- Section 3 presents the components of the ACSM and its relationship with other contrail formation and impact models.

- Section 4 describes a computational contrail RF method proposed by Schumann et al. Contrail coverage computed from ACSM can be converted into instantaneous RFs using Schumann's method.
- Section 5 provides a calibration of the ACSM model and presents results to show its fidelity compared to the results from other models for similar scenarios. It includes studies and analysis by applying Schumann's RF computational method to ACSM.
- Section 6 shows results from a case study using ACSM to estimate contrail RF as a function of time and space for 24-hrs of simulated air traffic over the United States.

2. Life Cycle of Contrails

Aircraft-induced contrails experience some common but complicated dynamical and cloud microphysical processes in a broad temporal and spatial range as summarized in Table 1. Initial contrails consist of a mixture of millions of super cooled water droplets and ice particles with most sizes less than $10\ \mu m$. In the next one or two minutes immediately after contrail formation, the water-droplets and ice particles are downwashed up to a few hundred meters by engine exhausts and wingtip vortices. After the downwash process, some water droplets and ice particles will be lost and the rest will aggregate into a linear-shaped cloud with initial length, depth, and width in meter scale, which persists in the ice-saturated environment. Contrails will sublime in ice sub-saturated atmospheric conditions. Most contrails will finally dissipate when ice content is below a certain threshold, while the rest transform into contrail cirrus which can last for many days and months just like natural cirrus clouds.

The life cycle of contrails can be simulated by modeling the processes with appropriate parameters as depicted in Fig. 1. There are several models of these processes in the contrails and atmospheric sciences literature and these models vary from simple empirical values to complex transport models involving atmospheric chemistry and physics. ACSM borrows freely from this literature and the next sections describe three models that have heavily influenced the development of ACSM and the simplifications to the processes as identified in Fig. 1.

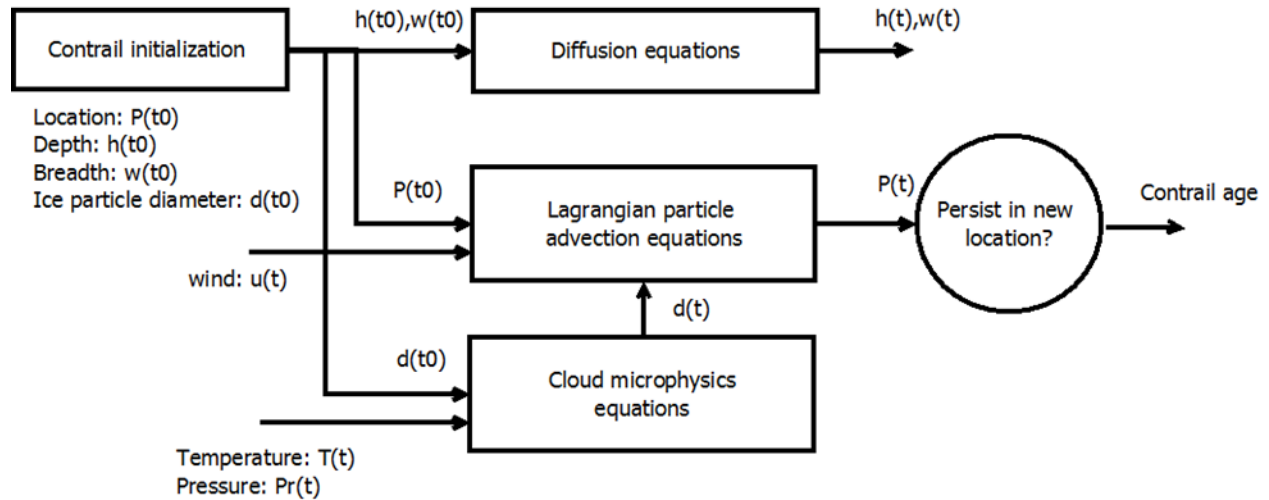


Figure 1. ACSM model structure

2.1 Stanford's Aircraft Contrail Model

Naiman and Lele *et al.* at Stanford University developed a two-phase approach to simulate the full life cycle of contrails [5], [6], [7], [8]. A large eddy simulation (LES) was developed to simulate aircraft contrail formation over the first twenty minutes, which provides an estimation of initial contrail cloud coverage areas and optical depths at various atmospheric conditions. Optical depth describes how transparent a cloud is or how much the cloud modifies light passing through it. Its value not only depends on the thickness of the cloud but also the humidity and temperature of the cloud. Its value is dimensionless. A larger value of optical depth means less light passing through the cloud. Thin clouds at a very low temperature like aviation-induced contrails are optically thin,

i.e., have small optical depth. To reduce the computational intensity, a low order contrail model was developed to model young-age contrail transport given inputs from LES.

2.2 Burkhardt-DLR Aircraft Contrail Model

Burkhardt and Karcher at the DLR developed a contrail cirrus cloud model based on physical processes [9]. The contrail cirrus cloud is represented by its fractional coverage (b), length (l), and ice-water mass mixing ratio (ω_{ice}). The dynamic processes include formation, transport, spreading, deposition, sublimation, and precipitation. The model also incorporates natural cirrus clouds, which compete with aircraft-induced contrail cirrus clouds for water vapor.

Equations (1) (Eqns. (1)-(3) from [9]) demonstrate dynamical processes of the Burkhardt-DLR contrail model.

$$\begin{aligned}\frac{\partial b}{\partial t} &= \left(\frac{\partial b}{\partial t}\right)_{transport} + \left(\frac{\partial b}{\partial t}\right)_{spread} + \left(\frac{\partial b}{\partial t}\right)_{sublimation} + \left(\frac{\partial b}{\partial t}\right)_{new} \\ \frac{\partial l}{\partial t} &= \left(\frac{\partial l}{\partial t}\right)_{transport} + \left(\frac{\partial l}{\partial t}\right)_{sublimation} + \left(\frac{\partial l}{\partial t}\right)_{new} \\ \frac{\partial \omega_{ice}}{\partial t} &= \left(\frac{\partial \omega_{ice}}{\partial t}\right)_{transport} + \left(\frac{\partial \omega_{ice}}{\partial t}\right)_{deposition} + \left(\frac{\partial \omega_{ice}}{\partial t}\right)_{precipitate} + \left(\frac{\partial \omega_{ice}}{\partial t}\right)_{new}\end{aligned}\quad (1)$$

Figure 2 shows structure of Burkhardt-DLR's aircraft contrail model based on Eqn. (1). The main structural differences between this model and the ACSM are highlighted in dotted rectangles and arrows. The sublimation process is not modeled in ACSM.

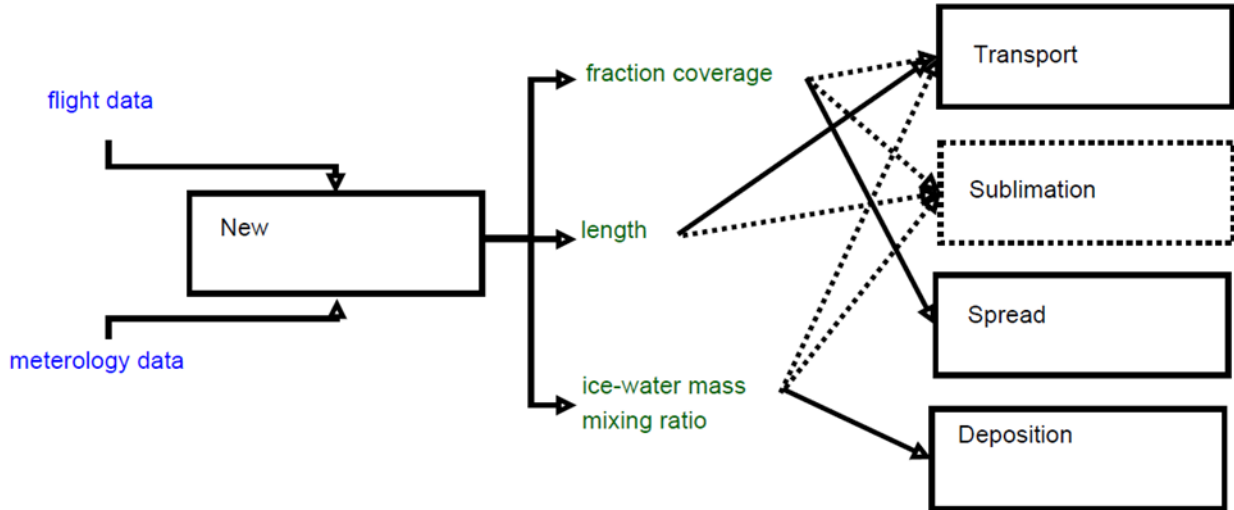


Figure 2. Burkhardt-DLR's aircraft contrail model structure (dotted boxes and arrows represent the additional modules and processes compared to ACSM)

2.3 CoCiP-DLR Aircraft Contrail Model

A contrail cirrus prediction tool (CoCiP) was also developed at DLR [10], [11]. Given inputs of aircraft trajectories and weather forecast data, CoCiP calculates instantaneous RF resulting from aircraft contrails. CoCiP is arguably the most comprehensive software tool to simulate the full life cycle of aircraft-induced linear contrails and contrail cirrus today. ACSM is generally designed to

share many similar basic properties with CoCiP, such as model parameters and cloud climate model, but with reasonable modification and simplification, as highlighted below:

1. CoCiP calculates contrails per each aircraft trajectory, while ACSM calculates contrails by aircraft occupancy in a gridded airspace.
2. CoCiP models the contrail cross-sectional area as an ellipsoid with Gaussian density distribution. ACSM assumes a uniform density for a rectangular cross-sectional area, which should improve computational efficiency. In addition, ACSM does not consider the contrail cross-section tilting due to vertical wind shear. Generally speaking, cross-section tilting reduces cloud effective depth and thus cloud optical depth.
3. Immediately following formation, contrail ice particles will be down washed by the aircraft wingtip wake vortex over the first one or two minutes. The wake vortex downwash process determines individual contrail cloud coverage areas and location as well as ice particle numbers and sizes depending on aircraft type, performance parameters such as airspeed and fuel flow rate, and the ambient atmospheric conditions. Such a wake vortex downwash process was modeled in CoCiP, but not modeled in ACSM. To compensate, ACSM uses average contrail cloud coverage areas, ice particle sizes, and assumptions of the number of post-downwash ice particles as initial parameters that are based on data from CoCiP and found elsewhere in the literature. Given that the size of airspace grid cells is much greater than the contrail ice particle downwash relocation distance, it is reasonable to assume that newly formed contrail ice particles remain in the same grid cell after downwash processes in ACSM.
4. For simplification, ACSM assumes a spherical ice particle shape throughout the contrail lifetime. It is well understood by cloud microphysicists that shapes of ice particles (ice-cloud particle habits) vary by temperature. Ice particles at different temperatures would have different shapes and microphysical properties, and finally cause different RF.

3. Ames Contrail Simulation Model

This section provides detailed descriptions of the modules in ACSM and discusses the differences between ACSM and other models available in the literature.

3.1 Contrail Formation

Aircraft contrail formation conditions have been relatively well understood, which is an atmospheric thermodynamics process based on the Schmidt-Appleman criterion [12] [13] [14]. Among the many causes of aircraft contrail formation, the commonly accepted main cause is a thermodynamic process called “heterogeneous nucleation,” that results when engine-emitted water vapor condenses into super cooled water liquid droplets with subsequent freezing at a lower supersaturation value due to the addition of engine-emitted cloud forming particles (soot) or cloud condensation nuclei. Aircraft contrails form at high altitudes that are frost-saturated (i.e., supersaturated with respect to ice but subsaturated with respect to water). Persistent contrails may form when aircraft fly through a region of airspace, where ambient temperature and relative humidity with respect to water and ice satisfy all of the following inequalities:

$$\begin{cases} RH_w > r_{contr}, \\ T < T_{contr}, \\ RH_i > 100\%, \text{ and} \\ RH_w < 100\% \end{cases} \quad (2)$$

where RH_w is ambient relative humidity with respect to water and T is ambient temperature. They can be extracted from meteorological data such as National Oceanic and Atmospheric Administration (NOAA)'s Rapid Update Cycle (RUC) or Rapid Refresh (RAP). RH_i is relative humidity with respect to ice that can be derived from RH_w as follows:

$$RH_i = RH_w \frac{6.0612 \exp(18.102T/(249.15 + T))}{6.1162 \exp(22.577T/(273.78 + T))}. \quad (3)$$

r_{contr} and T_{contr} are critical relative humidity and temperature respectively, calculated as follows:

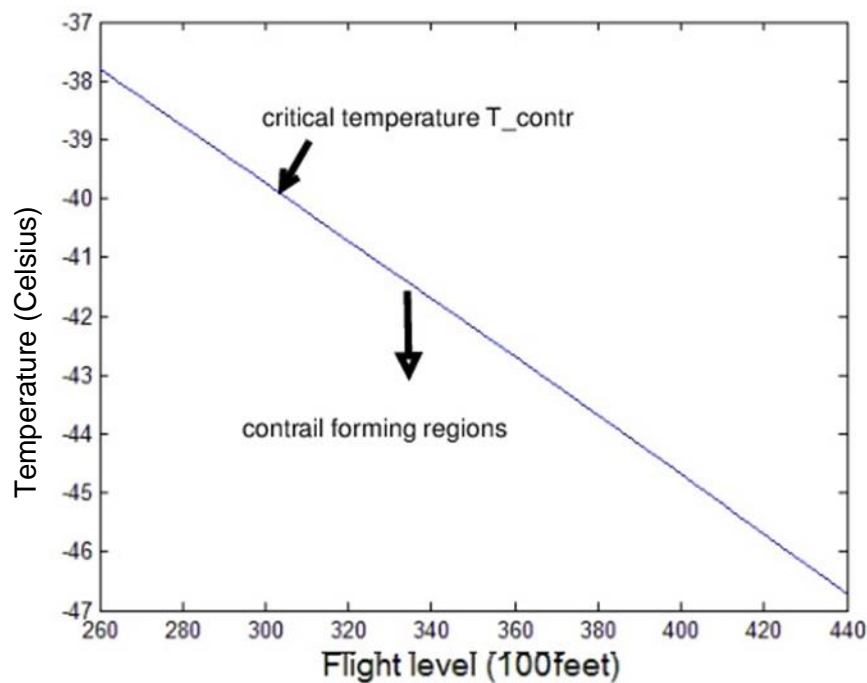
$$T_{contr} = -46.46 + 9.43 \ln(G - 0.053) + 0.72 \ln^2(G - 0.053) + 273.15, \quad (4)$$

$$r_{contr} = \frac{G(T - T_{contr}) + e_{sat}^{liq}(T_{contr})}{e_{sat}^{liq}(T)} \quad (5)$$

where the unit of temperature is Celsius, $e_{sat}^{liq}(T) = 6.0612 \exp\left(\frac{18.102T}{249.52+T}\right)$ and $G = \frac{EI_{H_2O}C_pPr}{\epsilon Q(1-\eta)}$. $EI_{H_2O} = 1.25$ is water vapor emission index, $Q = 42 \times 10^6 J/kg$ is combustion heat per unit mass of jet fuel, $C_p = 1.004 \times 10^3 J/kgK$ is air heat capacity, Pr is ambient pressure that can be also extracted from meteorological data, $\epsilon = \frac{M_{H_2O}}{M_{air}}$ is the ratio of molar masses of water and dry air,

and $\eta = 0.3$ is the average propulsion efficiency of the jet engine.¹

Figures 3 and 4 show the feasible ambient temperatures and relative humidity with respect to water for contrail formation at different flight levels assuming standard temperature and pressure at sea level based on the Schmidt-Appleman criterion. The following observations can be made from Figures 3 and 4: (a) Contrails are formed in cold ambient air, typically below -40°C and above 30,000 feet; and (b) Contrails are formed in humid ambient air, typically with relative humidity with respect to water greater than 50%. The required relative humidity threshold for contrail formation decreases as ambient temperature decreases. Contrail formation requires less water vapor in the ambient air at higher altitudes (but below the tropopause).



¹ The propulsion coefficient can also be computed for individual aircraft given aircraft speed and engine parameters. Studies show that as the engine propulsion coefficient η increases (e.g., modern aircraft), the critical temperature increases by a rate about 1.4 Kelvin per 10% increment in η enabling the potential to form contrails at lower altitudes [12].

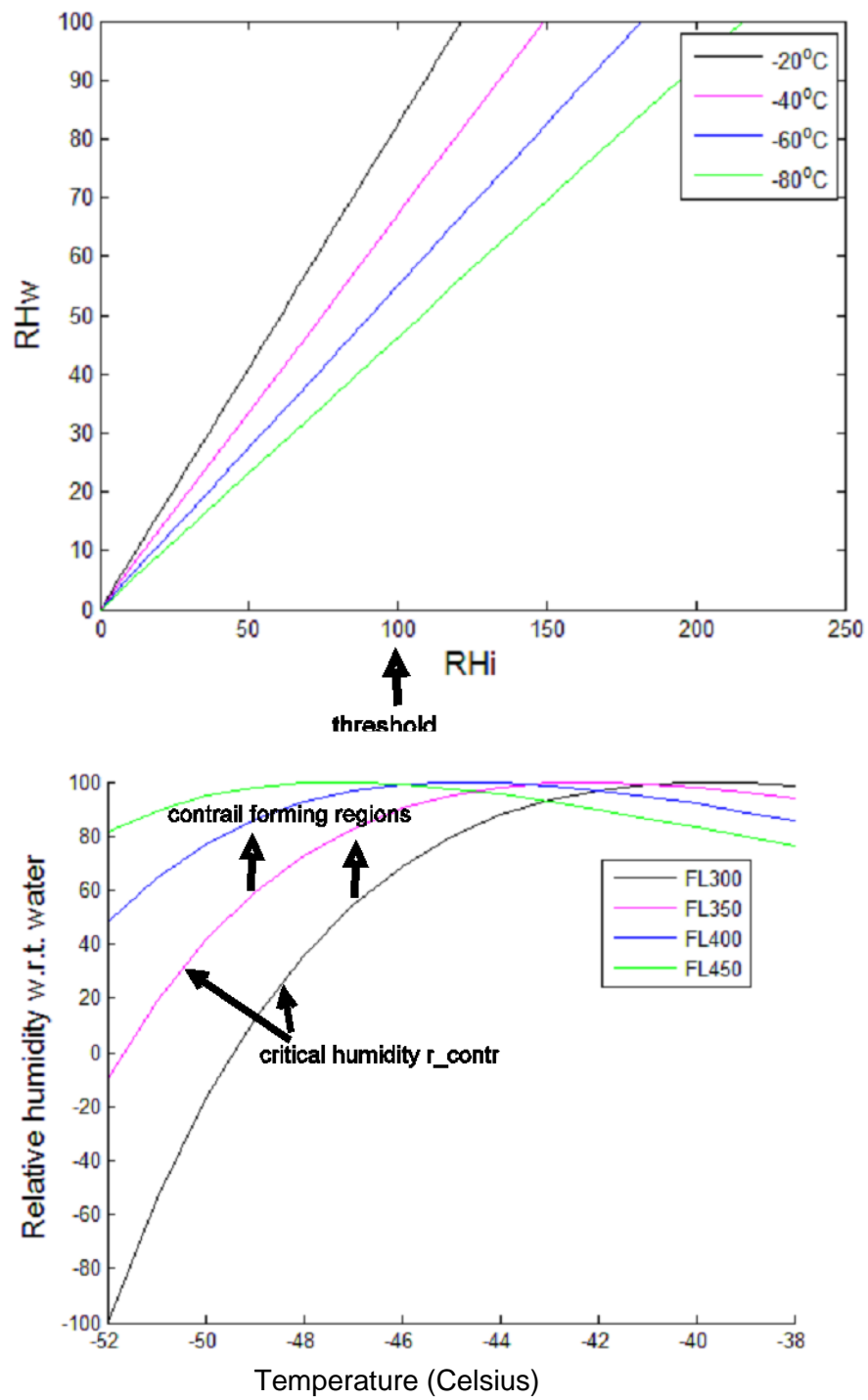


Figure 3. Relationship among contrail-formation meteorological parameters

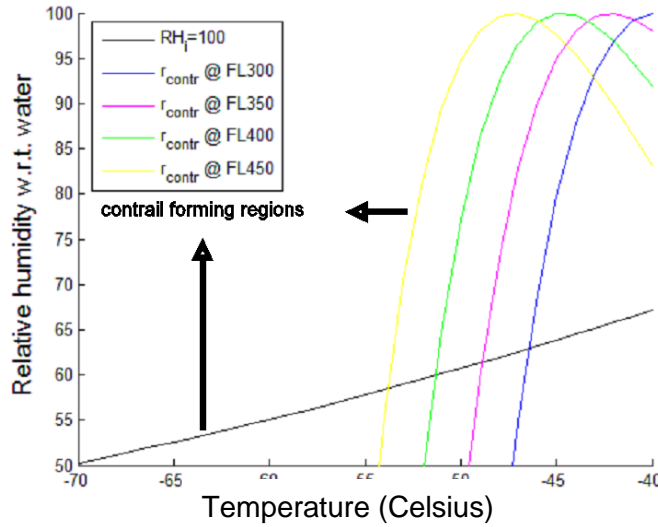


Figure 4 Feasible ambient relative humidity w.r.t water for contrail forming

Figure 5, called the Appleman Diagram, is from Schumann's paper [12], where the dotted lines represent critical temperatures T_{LC} for contrail formation (but not persistence of contrails) at various relative humidity values. From Fig. 5, contrails can be formed in less humid environments given significantly low ambient temperature. Comparing Eq. (2) with Eq. (8), Eq. (2) added the additional conditions that require the ambient air to be frost-saturated ($RH_w < 100\%$ and $RH_i > 100\%$). These additional conditions ensure that contrails to be considered in ACSM can persist over the initial formation period for at least twenty minutes in order to have a meaningful impact on global climate.

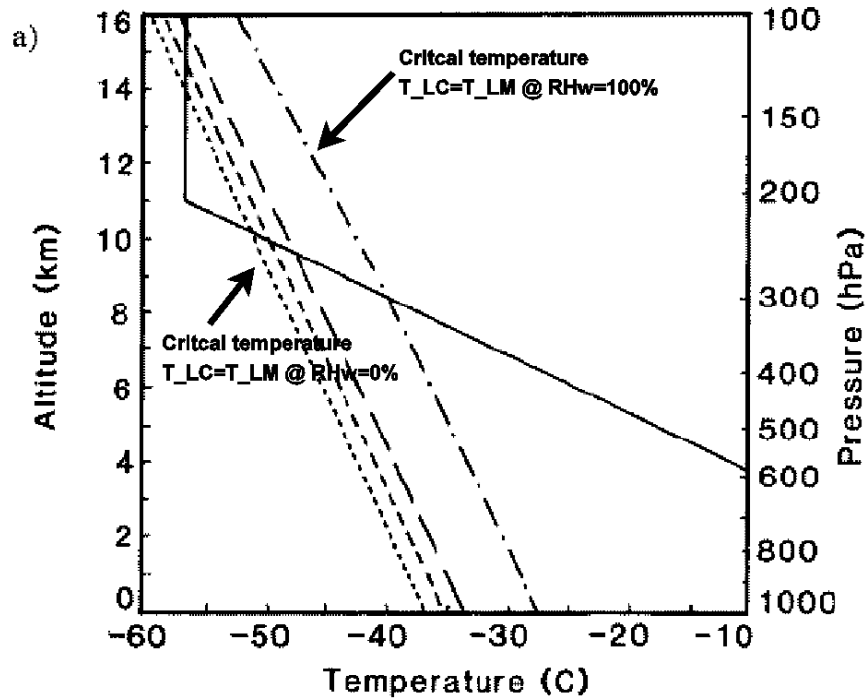


Figure 5. Appleman diagram from [12]

Some final comments are:

1. The critical temperature T_{LC} from Fig. 5 is a function of relative humidity RH_w while T_{contr} in Fig. 3a is independent on RH_w . Moreover, T_{contr} equals to T_{LM} (or equivalently, T_{LC} when $RH_w = 100\%$).
2. CoCiP uses a different equation from Eqn. (3) to represent the relation between RH_i and RH_w as follows (T is Kelvin):

$$RH_w = RH_i \frac{100 \exp [-6096.94/T + 16.64 - 0.027T + 1.674(10^{-5})T^2 + 2.434 \ln T]}{100 \exp [-6024.53/T + 24.722 + 0.0106T - 1.32(10^{-5})T^2 - 0.494 \ln T]} \quad (6)$$

As shown in Fig. 6, the two representations are consistent.

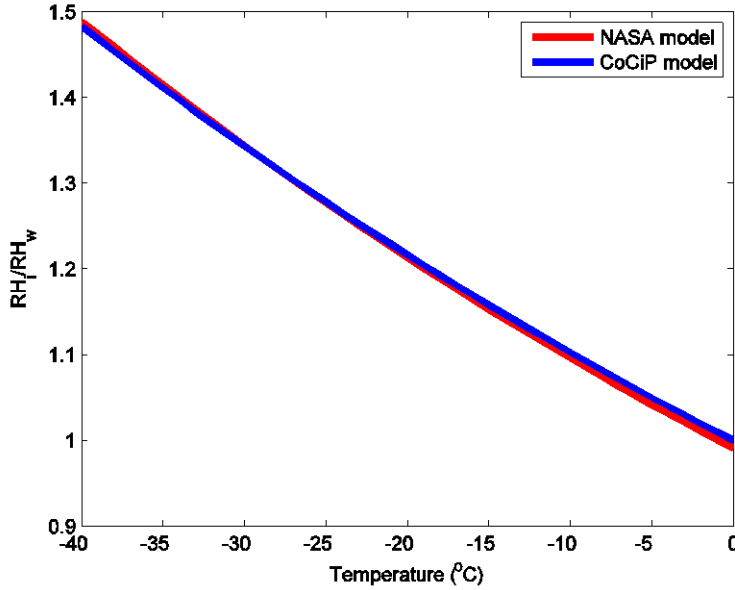


Figure 6. Ratio between relative humidity over ice and relative humidity over water

In summary, all investigated aircraft contrail models including ACSM use the same principle of Appleman's criteria to determine contrail formation. Given any region of airspace centered at (x =latitude, y =longitude, z =altitude) and within a time interval around t , if ambient relative humidity $RH_w(x, y, z, t)$, $RH_i(x, y, z, t)$ and ambient temperature $T(x, y, z, t)$ satisfy Eqn. (2), persistent contrails will form immediately following an aircraft flying through that region.

3.2 Contrail Persistence and Age

Aircraft contrails persist in an ice-saturated atmosphere, wherein:

$$RH_i > RH_{ic}, \quad (9)$$

where the critical value RH_{ic} is normally set between 80%-100% in order to preserve continuity of the contrail persisting areas. Let $\Omega(t)$ represent the collection of contrails persisting areas at t that satisfy Eqn. (9). For any given contrail $\{p(t), t \geq t_0\}$ (t is contrail age, t_0 is contrail forming time), the maximum age or life span of contrails LS_c is defined as follows:

$$LS_c(p(t)) = t_f - t_0, \quad (10)$$

where

$$t_f = \min\{t \geq t_0 | p(t) \notin \Omega(t)\}.$$

3.3 Wake Vortex Turbulence Model

In the few minutes immediately after contrail ice particles are formed based on the Schmidt-Appleman criterion, those particles will be downwashed due to aircraft wingtip wake vortex turbulence. The downwash process determines initial contrail cloud coverage, microphysical properties such as optical depth, and locations through a complex fluid dynamics process that can be modeled by Large Eddy Simulations [7]. In ACSM, such downwash processes have not been modeled. The main reason is that the downwash process only takes a few minutes. During this period, ice particles are displaced at most a few hundred meters vertically and tens of meters horizontally from aircraft engines. Such displacement distances are far less than the normal grid cell size (13km for RUC/RAP data) used in ACSM. In ACSM, initial contrail cloud parameters such as depth and width are set to constant values based on either computer simulations or field observations [8] [13] [14]. For computational simplicity, it is assumed that variations in initial contrail cloud parameters computed with high fidelity simulations of downwash processes would have a relatively negligible impact on the total contribution of long-term climate change (radiative forcing).

3.4 Contrail Initial Shape and Concentration

In Stanford's and DLR's CoCiP models, initial contrail shape and ice crystal concentration are related to specific aircraft type. In Stanford's model [Fig. 7 (b)], initial contrail cross-section area was calculated based on total engine-emitted mass as follows:

$$A = \frac{\dot{m}_f}{\rho_a V_{TAS}} \alpha, \quad (11)$$

where $\rho_a = \frac{p}{R_a T}$ is air density, \dot{m}_f is fuel mass flow rate, V_{TAS} is airspeed, and α is a diffusion factor. This assumes that ice particle concentration is uniformly distributed along the cross-section.

In CoCiP [Fig. 7 (c)], initial contrail depth, width, and density (ice-water mass concentration) are calculated following the wake vortex downwash processes. Based on CoCiP's simulation (Fig. 4 from [11]), the initial depth generally varies between 30-140 meters with the majority around 80-120 meters, and the initial width varies between 0-20 meters with the majority around 5-15 meters.

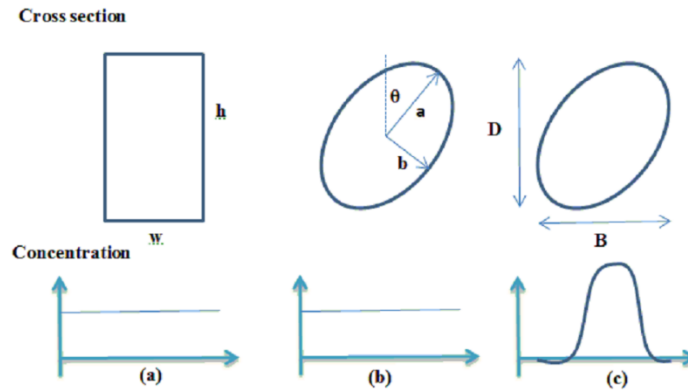


Figure 7. Contrail cross-section shapes: (a) rectangle with uniform concentration used in ACSM; (b) ellipse with uniform concentration used in Stanford's model; (c) ellipse with Gaussian distributed concentration used in CoCiP mode

The cross-section mass concentration of a contrail cloud in Fig. 7 (b) is represented by a normal distribution in CoCiP:

$$c(X) = \frac{C_0}{A} \exp \left\{ -\frac{1}{2} X^T \sigma^{-1} X \right\}, \quad (12)$$

where $X = [y \ z]$ are displacements along major and minor axes of ellipsoid contrail cross-sectional area or along width and depth axes of rectangular contrail cross-sectional area, and σ is a covariance matrix in the form:

$$\sigma = \begin{bmatrix} \sigma_{yy} & \sigma_{yz} \\ \sigma_{yz} & \sigma_{zz} \end{bmatrix},$$

where σ_{yy} and σ_{zz} are diffusion coefficients in horizontal and vertical directions of cross-section area, respectively.

The initial contrail cross-section width, depth, and area in Fig. 7 (c) are calculated by:

$$B = \sqrt{8\sigma_{yy}}, D = \sqrt{8\sigma_{zz}}, \text{ and } A = 2\pi\sqrt{\det(\sigma)}. \quad (13)$$

The initial ice mass mixing ratio (I_0 , mass of ice crystals per unit mass of air) used in CoCiP is equal to the total engine-emitted water vapor mass, which is an approximation without considering the amount of ice-saturated water vapor available in the ambient air nor the ice mass loss during wake vortex downwash sinking processes.

$$I_0 = \frac{m_{water}}{m_{air}} = \frac{\dot{m}_f}{\rho_a V_{TAS} A} EI_{H_2O}, \quad (14)$$

where EI_{H_2O} is the engine water emission index defined as kilogram water vapor per kilogram fuel burn and A is the contrail cloud cross-section area.

The initial ice crystal number concentration (N_0 , number of ice crystals per contrail length) is mainly determined by the number of emitted engine soot particles. The concentration is also influenced by nucleation. CoCiP considers ice particle loss during the wake vortex downwash processes,

$$N_0 = \alpha \frac{\dot{m}_f}{V_{TAS}} EI_{soot}, \quad (15)$$

where α is survival factor depending on aircraft type and meteorology conditions, which varies between [0.9-1] in accordance with CoCiP (Fig. 5 in [11]).

Accordingly, ice crystal number concentration per volume is $n_0 = N_0/A$ (particles/ m^3). Finally, total mass of contrail ice crystals per contrail length is computed by:

$$M_i = \frac{\dot{m}_f}{V_{TAS}} EI_{H_2O} = I_0 \rho_a A \quad (16)$$

In ACSM [Fig. 7 (a)], contrail cross-sections are modeled as a rectangle with uniform ice particle concentration for computational efficiency. It assumes that all contrails after downwash processes would have the same initial cross-section shapes.

Some comments are:

1. ACSM uses average values suggested by CoCiP. The initial contrail width and depth are chosen to be $w = 10m$ and $h = 100m$. The initial contrail cloud width is less than its initial depth.
2. Studies show that $EI_{soot} = EI_{PMNV} \approx 4(10^{14})$ black carbon particles per kg-fuel consumption for aircraft cruising above 30,000 feet on average. Also, aircraft normally cruise between 400-600 knots (or 205-308m/s). Fuel consumption rate varies by aircraft type. A gross estimation is between 4000-6000kg-fuel/hour (1.1-1.7kg/s) for twin-engine turbojet commercial airplanes. Using average aircraft cruise speed at 257m/s and fuel flow rate at 1.4kg/s, a gross estimation of initial ice particle number concentration is approximately 10^{12} per meter contrail length using Eqn. (15) (or 10^9 per unit air volume given initial contrail cross-section area $A = 1000m^2$). Similarly, average initial single ice crystal mass can be calculated using Eqn. (14) which is approximately 10^{-15} kg per particle given $EI_{H_2O} = 1.3kg/kg\text{-fuel}$. For spherical-shaped ice crystals, initial ice crystal diameter, d_i , is related to I_o and N_o by $d_i = 2\sqrt[3]{\frac{3}{4\pi} \frac{M_i}{N_o \rho_i}} \approx 10^{-6}m = 1\mu m$.

3.5 Advection Model

Contrails, consisting of small ice particles, are transported through the airspace driven by local winds. Let $p(t) = [x(t) \ y(t) \ z(t)]^T$ represent the contrail cloud mid-point (or endpoints) position at t , $u(p(t), t) = [x_w(p(t), t) \ y_w(p(t), t) \ z_w(p(t), t)]^T$ represent wind velocity vector at location $p(t)$ and time t . The notation $u(t) = [x_w(t) \ y_w(t) \ z_w(t)]^T$ is used for simplicity. The advection of linear contrails is calculated using the following standard Lagrangian dispersion equations:

$$\begin{cases} x(t + \Delta t) = x(t) + x_w(t)\Delta t, \\ y(t + \Delta t) = y(t) + y_w(t)\Delta t, \text{ and} \\ z(t + \Delta t) = z(t) + (z_w(t) + z_s(t))\Delta t, \end{cases} \quad (17)$$

where Δt is sample time, and z_s is ice particle settling velocity (or terminal velocity) based on Stokes' Law [15].

$$z_s(t) = -g\rho_i d_i^2(t)/18\eta, \quad (18)$$

where ρ_i is ice density, d_i is ice particle diameter, η is gas viscosity coefficient, and g is gravitational acceleration.

In CoCiP, a second correction step following Eq. (17) is added to improve accuracy given a large time step ($\Delta t = 1\text{hour}$):

$$X_{new}(t + \Delta t) = X(t) + \frac{\Delta t}{2} \left(\frac{\partial}{\partial t} X(t) + \frac{\partial}{\partial t} X(t + \Delta t) \right), \quad (19)$$

where $X(t) = [x(t) \ y(t) \ z(t)]^T$ and

$$\frac{\partial}{\partial t} X(t) = [x_w(t) \ y_w(t) \ z_w(t) + z_s(t)]^T.$$

Correction steps can be added in ACSM if necessary.

Some comments are:

1. The vertical wind velocity is an important factor in contrail evolution and is often measured by the pressure tendency provided in some meteorological data such as the RUC numerical weather prediction model. The relationship between pressure tendency and vertical velocity is represented by:

$$\omega \triangleq \frac{dp}{dt} = -g\rho_a z_s. \quad (20)$$

2. Figure 8 shows the single ice particle terminal velocity increment over its diameter using Stokes' equation (18). By comparing with some empirical data such as Fig. 10-42 on Pg. 438 of [16] and Fig. 8 from [11], it is observed that the Eqn. (18) formulation agrees well with empirical data (values are in the same numerical order) only for small ice particles ($d_i \leq 100\mu m$). The agreement is far less consistent for large ice particles $d_i > 100\mu m$. This observation is in accordance with prerequisite conditions of Stokes' law, which is stated to be applied only for spherical particles with very small Reynolds numbers (i.e., very small particle sizes).

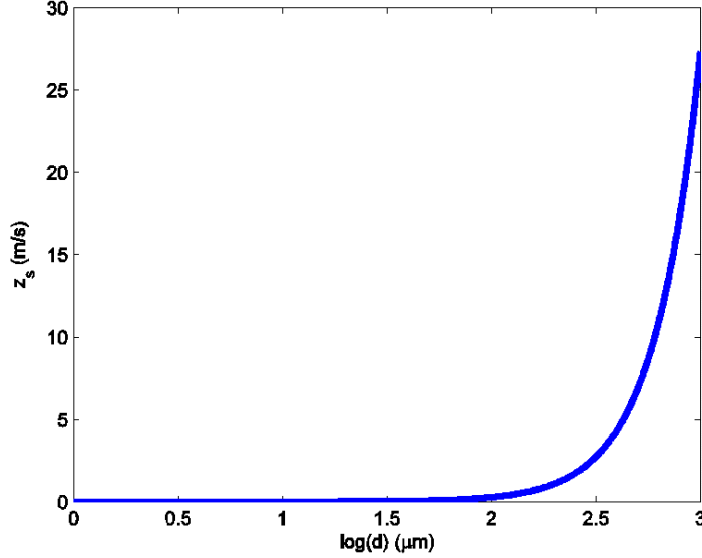


Figure 8. Single ice particle terminal velocity over diameter using Eqn. (18)

To overcome such discrepancies while still maintaining computational efficiency, ACSM uses an empirical equation from [16] to calculate terminal velocity for large ice particles with diameter $d_i > 100\mu m$ and Eq. (18) for small ice particles with $d_i \leq 100\mu m$, as shown in Fig. 9. By comparing Fig. 8 with Fig. 9 or their corresponding equations, terminal velocities for relatively large ice particles grow linearly with respect to size (diameter) as:

$$z_s = \begin{cases} -g\rho_i d_i^2(t)/18\eta, & d_i \leq 100\mu m \\ -9(100d_i)^{0.8}, & d_i > 100\mu m, \end{cases} \quad (21)$$

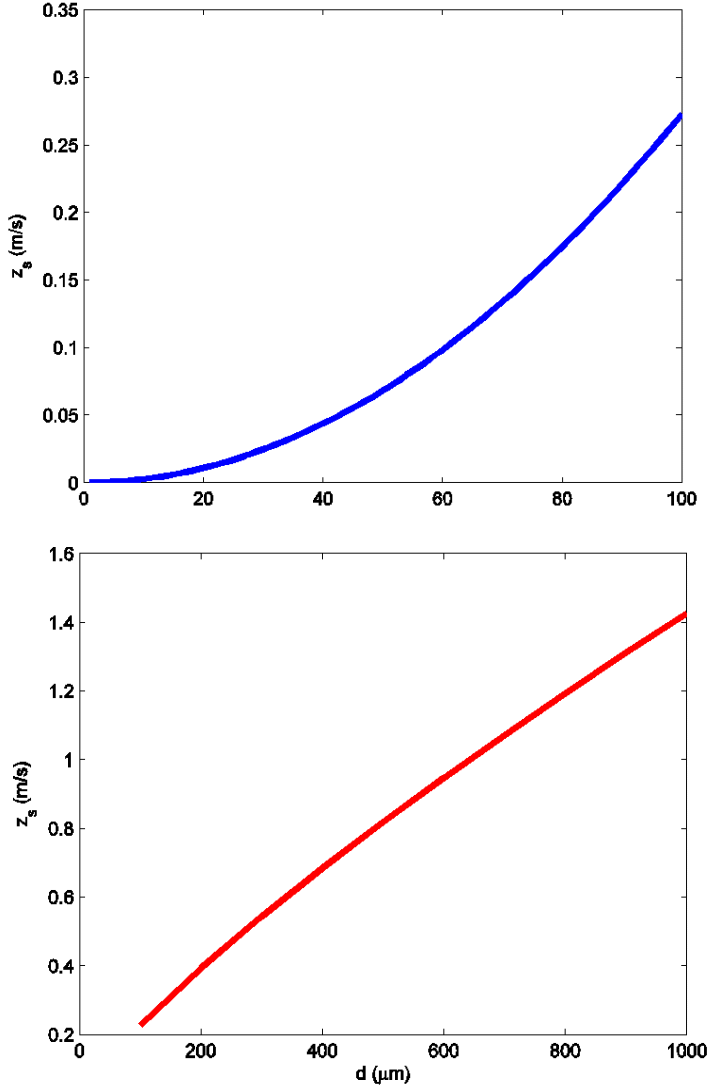


Figure 9. Single ice particle terminal velocity over diameter using Eqn. (21): (top) $d_i \leq 100 \mu m$; and (bottom) $d_i > 100 \mu m$

3.6 Diffusion Model

Contrails can spread or diffuse in both vertical and horizontal directions because of turbulent mixing and wind shear. In ACSM, contrail spread is computed using standard diffusion equations:

$$\begin{aligned} \frac{dh(t)}{dt} &= \frac{D_v}{h}, \\ \frac{dw(t)}{dt} &= \frac{D_h}{w}, \end{aligned} \quad (22)$$

where $h(t)$ is contrail cross-section depth, $w(t)$ is width, and D_h and D_v are constant diffusion coefficients in horizontal and vertical directions respectively. Based on field experiments conducted by Schumann *et al.* [13], D_v is estimated to vary between $0-0.6 m^2/s$ and D_h is estimated to vary between $5-20 m^2/s$ at aircraft cruising altitudes (near tropopause) after initial contrail forming and downwash processes. In ACSM, these variables are not allowed to exceed predetermined upper limits (i.e., $D_h = 20 m^2/s$ and $D_v = 0.6 m^2/s$).

In Stanford's model, contrail cross-section rotation due to wind shear is also considered in addition to diffusion. The model can be summarized as follows:

$$\begin{aligned}\frac{d\theta}{dt} &= \frac{\partial u_s}{\partial z} \cos \theta, \\ \frac{da}{dt} &= \frac{D_a}{a} + a \frac{\partial u_s}{\partial z} \sin \theta \cos \theta, \text{ and} \\ \frac{db}{dt} &= \frac{D_b}{b} - b \frac{\partial u_s}{\partial z} \sin \theta \cos \theta,\end{aligned}\tag{23}$$

where a , b and θ are ellipse parameters as shown in Fig. 7, $\frac{\partial u_s}{\partial z}$ is the vertical wind-shear component (i.e., vertical gradient of horizontal wind velocity) projected onto the contrail cross-section plane. In Stanford's model, wind shear causes contrail cross-section tilt at $\theta(t)$ in addition to width and depth spread. Note that Eqn. (22) is a special case of Eqn. (23) without considering wind shear (i.e., $\frac{\partial u_s}{\partial z} = 0$).

In the Burkhardt-DLR model and the CoCiP model, wind shear is also considered. Contrail diffusion without considering wind shear is computed using (Eqn. (29-31) from [11] or Eqn. (6) from [9]):

$$\begin{aligned}\sigma_{yy}(t + \Delta t) - \sigma_{yy}(t) &= 2D_H \Delta t \\ \sigma_{zz}(t + \Delta t) - \sigma_{zz}(t) &= 2D_V \Delta t\end{aligned}\tag{24}$$

where $\sigma_{yy} = B^2/8$ and $\sigma_{zz} = D^2/8$ are defined in Eqns. (12) and (13) (B and D are contrail cross-section width and depth). Note that Eqn. (24) is a discrete form of Eqns. (22), which can be rewritten in the continuous form as:

$$\begin{aligned}\frac{dB(t)}{dt} &= \frac{D_h}{B}, \\ \frac{dD(t)}{dt} &= \frac{D_v}{D},\end{aligned}\tag{25}$$

where $D_h = 8D_H$ and $D_v = 8D_V$.

3.7 Contrail Cloud Microphysics Model

Contrail cloud ice particles grow by the uptake of excessive water vapor in the surrounding air at temperatures below $0^\circ C$. By definition, a mechanism that causes cloud ice particle growth by diffusion of water vapor is called deposition. Deposition is a common dynamic process in cloud microphysics that has been well studied [16], [14]. For completeness, ice particle diffusional growth is presented in detail in this section. Note that ACSM assumes all ice particles are spherical-shaped throughout the entire linear contrail life cycle.

1. Let $r(t)$ (meter) be the single ice particle radius and $D_v(m^2/s)$ the diffusivity of water vapor at temperature between -40 and $40^\circ C$, where

$$D_v = 0.211 \left(\frac{T}{T_0} \right)^{1.94} \left(\frac{p_0}{P} \right) 10^{-4},\tag{26}$$

where T (Kelvin) is the reference temperature, $T_0 = 273.15K$ is the standard temperature, P (Pa) the reference pressure, and $p_0 = 11325Pa$ is the standard pressure.

Let λ (meter) be the mean free path of air molecules defined as

$$\lambda = \frac{2\mu}{p \sqrt{\frac{8m_{air}}{\pi RT}}},\tag{27}$$

where $\mu = 1.83 \times 10^{-5}$ is viscosity of air, $m_{air} = 0.018 \text{ kg/mol}$ is molecular mass of air, and $R = 8.214 \text{ (J/K)/mol}$ is the gas constant.

Then, the modified diffusivity of water vapor for kinetic correction is calculated by:

$$D'_v = \frac{D_v}{\frac{r(t)}{r(t)+\Delta_v} + \frac{D_v}{r(t)\alpha} \sqrt{\frac{2\pi M_w}{RT}}}, \quad (28)$$

where α is deposition coefficient, $\Delta_v = 1.3\lambda$ and $M_w = 0.018 \text{ kg/mol}$ is ratio of molecular mass of water and dry air.

Let κ'_a be the modified thermal conductivity of water vapor for kinetic correction.

$$\kappa'_a = \frac{\kappa_a}{\frac{r(t)}{r(t)+\Delta_T} + \frac{\kappa_a}{r(t)\alpha_T \rho_{air} c_p} \sqrt{\frac{2\pi M_w}{RT}}}, \quad (29)$$

where $\kappa_a = 0.025 \text{ J/s/m/c}$ is thermal conductivity of water vapor, thermal accommodation coefficient $\Delta_T = 2.16 \times 10^{-7} \text{ m}$, $\alpha_T = 0.7$, ρ_{air} is air density, and $c_p = 1 \times 10^3 \text{ J/kg/K}$ is specific heat of dry air.

Let $e_{sat,i} \text{ (Pa)}$ be the saturation vapor pressure with respect to ice given by

$$e_{sat,i} = e^{9.55 - \frac{5723.3}{T} + 3.53 \log(T) - 0.0073T}. \quad (30)$$

Let $e_{sat,w} \text{ (Pa)}$ be saturation vapor pressure with respect to water given by

$$e_{sat,w} = 611.2 e^{\frac{17.62(T-273.15)}{243.12 + (T-273.15)}}. \quad (31)$$

Let L_s be specific latent heat of sublimation computed as:

$$L_s = (2834.1 - 0.29T - 0.004T^2)10^3. \quad (32)$$

2. The mass diffusional growth rate of a single ice particle is calculated by:

$$\dot{m}(t) = \frac{4\pi C S_{V,i}}{\frac{RT\rho_i}{e_{sat,i} D'_v M_w} + \frac{L_s \rho_i}{\kappa'_a T} \left(\frac{L_s M_w}{RT} - 1 \right)}, \quad (33)$$

Where $C = r(t)$ is capacitance factor of a spherical ice particle, and saturation ratio of water vapor with respect to ice is $S_{V,i} = \frac{e_{sat,w}}{e_{sat,i}} - 1$.

3. Finally, the radius diffusional growth rate of a single spherical ice particle is calculated by:

$$\dot{r}(t) = \frac{\dot{m}(t)}{\rho_i 4\pi r^2(t)}. \quad (34)$$

Some comments are:

1. Regarding the Bergeron process ($e_{sat,w} > e > e_{sat,i}$): first, $e < e_{sat,w}$ creates sub-saturated environments for water droplets, which results in liquid water evaporation; second, $e > e_{sat,i}$ creates supersaturated environments for ice particles, which results in water vapor deposition. Combined in the two steps, liquid water is converted into ice particle growth in the Bergeron process.
2. Figure 10 depicts the relation between $S_{V,i}$ in Eqn. (33) and temperature. Note that if $T \leq 0^\circ C$, $S_{V,i} \geq 0$ (Bergeron process $e_{sat,w} > e_{sat,i}$) and thus $\dot{m} \geq 0$. If $T > 0^\circ C$, $\dot{m} < 0$. This indicates that ice particles grow when $T \leq 0^\circ C$ and shrink when $T > 0^\circ C$. Thus Eqn. (33) models both diffusion of water vapor (due to deposition) onto ice particles and diffusion of heat (due to sublimation) away from ice particle surface. Furthermore, Fig. 11 shows the normalized ice particle growth rate as a function of temperature. From the figure, it can be seen that ice particles do not grow monotonically with respect to temperature. The maximum ice particle growth rate occurs near $-15^\circ C$.

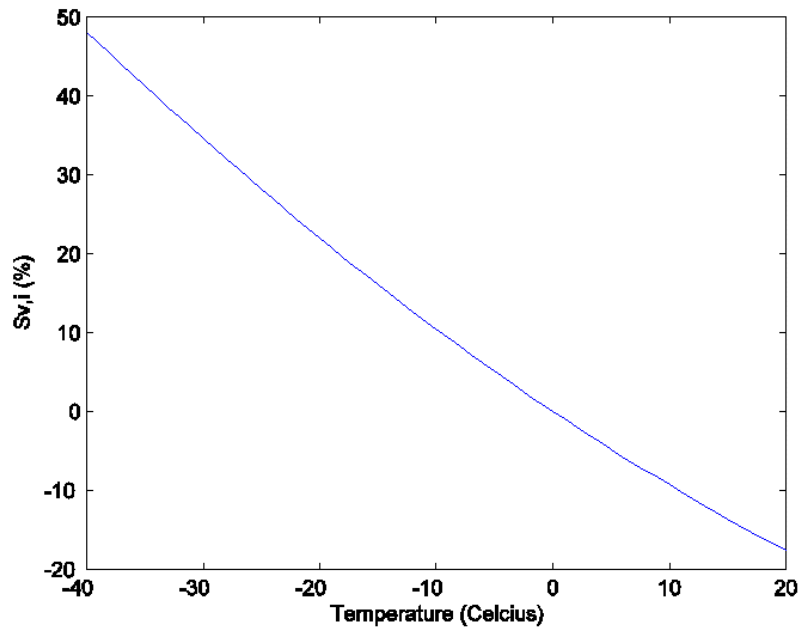


Figure 10. Saturation ratio of water vapor w.r.t ice $S_{V,i}$ over temperature

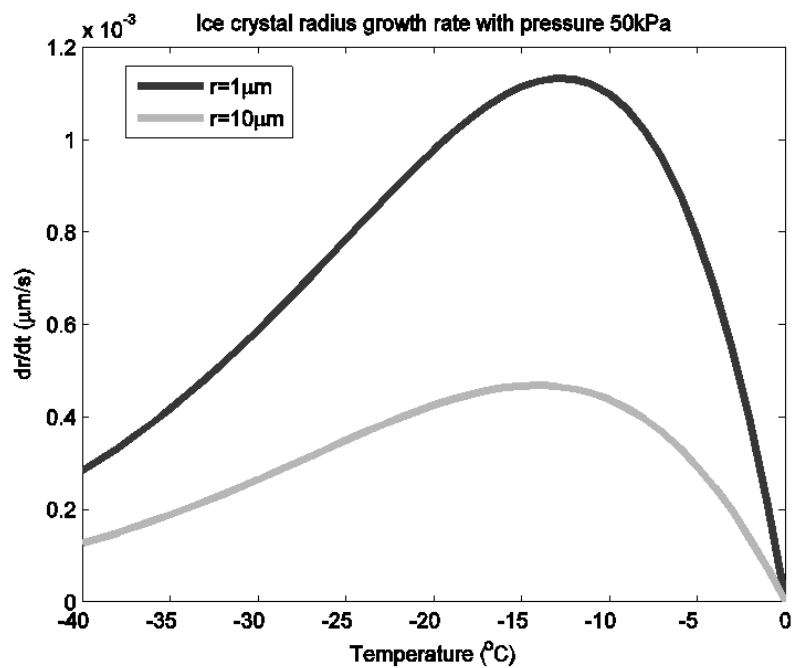
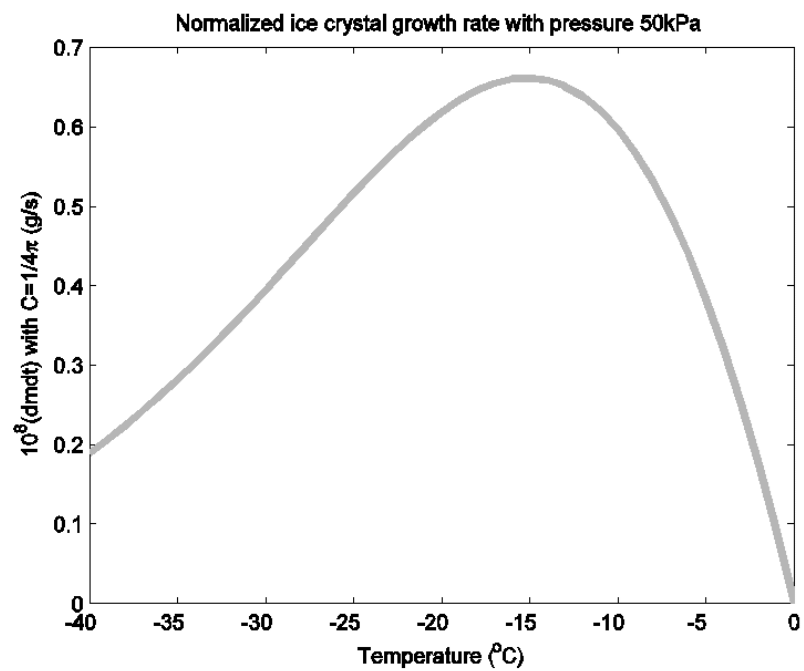


Figure 11. Contrail ice particle diffusional growth: (top) normalized mass growth rate; (bottom) radius growth rate

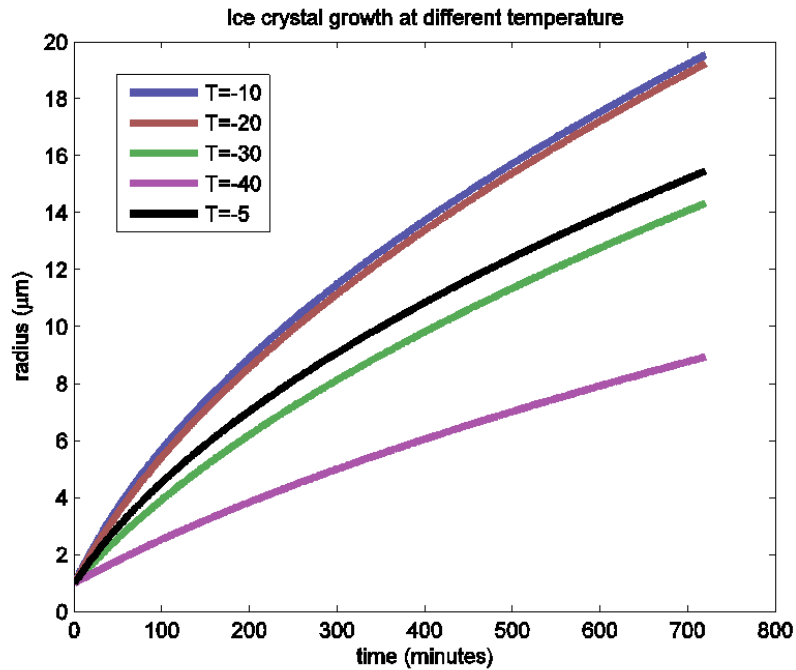


Figure 12. Contrail ice particle radius growth by deposition at pressure 50kPa over time, which is consistent with results from CoCiP (Fig. 7 in [11])

3. Other ice crystal growth models include collection, accretion, and/or melting [16]. These are not modeled in ACSM as their contributions to ice particle mass growth are very small compared to depositional growth. A more general discussion of various cloud ice particle growth processes can be found in [16].

4. Contrail RF

The overall scientific understanding of climate impact resulting from aviation-induced contrails (including linear contrails and contrail cirrus clouds) is listed as “low” in the 2021 IPCC assessment [4].

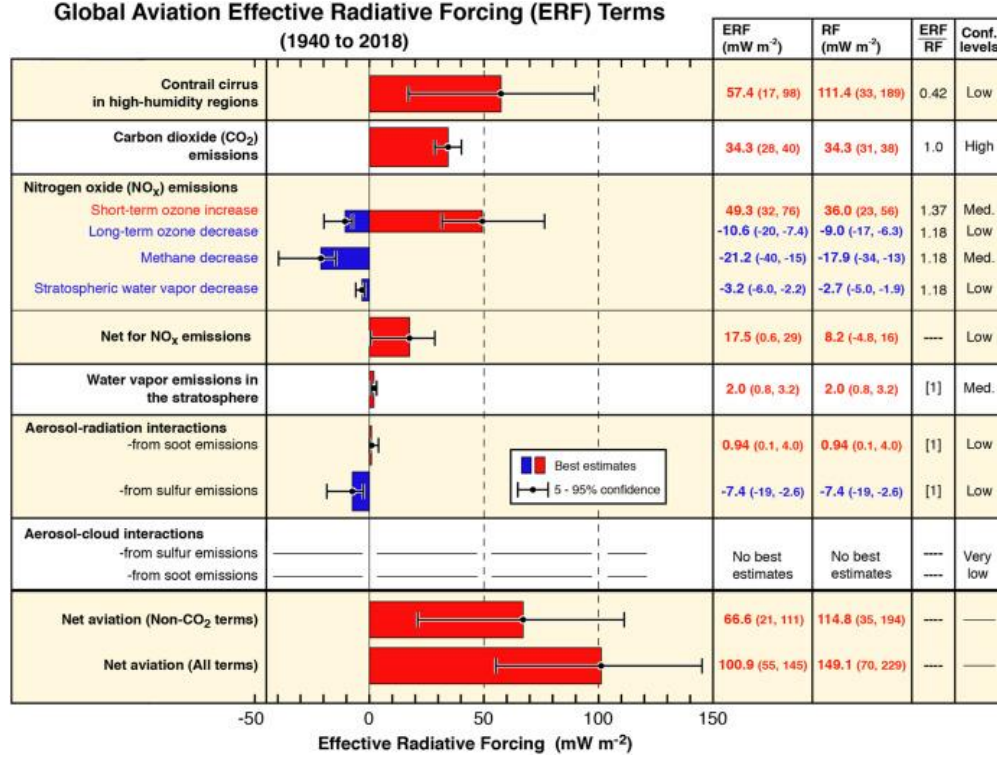


Figure 13. Estimated aviation RF for 2000 to 2018 based on IPCC studies

A common metric used to measure global temperature change is radiative forcing (RF). Aircraft-induced contrails cause both negative radiative forcing by reflecting incoming shortwave radiation and positive radiative forcing by trapping outgoing longwave radiation. Overall, contrails resulting from global aviation activities have a positive impact on global warming. An estimation of total RF resulting from aviation-induced linear contrails, as shown in Fig. 13, is 10mW/m² based on IPCC studies [2]. It contributes approximately 21% of total aviation RF in 2000 [18]. The same study estimated total RF from aviation CO₂ emissions and O₃ due to aviation NO_x emissions to be 25mW/m² and 22mW/m² respectively. The RF value due to contrails is updated to be 12mW/m² for 2005 with an uncertainty range of 5-26mW/m² [1]. The total RF impact would be much greater (in the range of 13-87mW/m²) if contrail cirrus clouds are included, which exceeds RF from aircraft CO₂ emissions. Next, the global mean surface temperature change ΔT_s (Kelvin) resulting from global mean radiative forcing change resulting due to contrails $\Delta RF_{contrails}$ is represented in a simple linear relation as follows:

$$\Delta T_s = \lambda \cdot \Delta RF_{contrails} \quad (35)$$

where, λ (K m²/W) is a constant climate sensitivity parameter.

The Aggregate Global Temperature Potential (AGTP) is commonly used to measure long-term global warming impact for greenhouse gas emissions. The AGTP per unit of radiative forcing due to aviation induced persistent contrails [19] that are sustained over a period H is calculated as follows:

$$AGTP^{contrails}(H) = \frac{1}{H} \int_0^H R(\zeta) d\zeta \quad (36)$$

where $R(\zeta)$ is the impulse response function of surface temperature change at ζ due to radiative forcing.

4.1 CoCiP RF model

Schumann et al. developed an empirical and computationally efficient method to compute aircraft contrail RFs [11], [20], [21] that was used in the development of CoCiP. CoCiP assumes that RF due to aircraft contrails represents a small perturbation relative to radiative fluxes at Top of Atmosphere (TOA). CoCiP computes instantaneous changes in net outgoing longwave (LW) and shortwave (SW) radiation induced by additional contrails, where outgoing LW radiation and SW radiation without contrails can be obtained from meteorological data. RF is represented as a function of contrail cloud optical depth and ambient temperature. It also depends on contrail ice particle size and contrail location (solar zenith angle). The methodology is presented in detail in the rest of this section.

CoCiP computes instantaneous changes in net longwave radiation RF_{LW} and shortwave radiation RF_{SW} induced by additional contrails as follows:

$$RF_{LW} = (OLR - \kappa_T(T_c - T_0))[1 - \exp\{-\delta_\tau F_{LW}(r)\tau\}]E_{LW}(\tau_c) \geq 0 \quad (37)$$

$$RF_{SW} = -SDR(t_A - A_{eff})^2 \alpha_c(\mu, \tau, r) E_{SW}(\mu, \tau_c) \leq 0 \quad (38)$$

where

$$F_{LW}(r) = 1 - \exp\{-\delta_{lr}r\} \quad (39)$$

$$E_{LW}(\tau_c) = 1 - \exp\{-\delta_{lc}\tau_c\} \quad (40)$$

$$\alpha_c(\mu, \tau, r) = R_c(\tau_{eff})[C_\mu + A_\mu R'_c(\tau_{eff})F_\mu(\mu)] \quad (41)$$

$$E_{SW}(\mu, \tau_c) = \exp\{\delta_{sr}\tau_c - \delta'_{sc}\tau_c/\mu\} \quad (42)$$

$$R_c(\tau_{eff}) = 1 - \exp\{\Gamma\tau_{eff}\} \quad (43)$$

$$R'_c(\tau_{eff}) = \exp\{-\gamma\tau_{eff}\} \quad (44)$$

$$F_\mu(\mu) = \frac{(1 - \mu)^{B_\mu}}{0.5^{B_\mu}} - 1 \quad (45)$$

where OLR (W/m^2) represents outgoing longwave radiation at TOA, SDR (W/m^2) represents solar direct radiation at TOA, μ represents cosine of Solar Zenith Angle (SZA), $A_{eff} = RSR/SDR$ represents effective albedo, RSR represents reflected solar radiation at TOA, $\tau_{eff} = \tau/\mu$ represents effective optical depth, τ represents contrail optical depth, τ_c represents contrail optical depth at $550nm$ and T_c (K) represents ambient temperature at the contrail location are directly provided or can be derived by meteorological data. Contrail ice particle radius r (μm) is computed using the contrail cloud microphysics model in Section 3.7. The values of 15 model fitting parameters are given in Appendix B.

Figure 14 shows RF_{LW} (longwave RF) and RF_{SW} (shortwave RF) values as a function of SZA. As seen in Figure 14, only shortwave RF described in Eqn. (38) varies with respect to SZA. Moreover, from Eqn. (38), the effective optical depth (τ_{eff}) causes a monotonic decrease of shortwave forcing as SZA increases until around $70^\circ - 80^\circ$. The inclusion of the function in Eqn. (45) is essential to describe the strong dependence of RF_{SW} for higher SZA. This dependence is known to be stronger for thin cirrus than for thick ones. And this factor is accounted for by multiplying the reflectance in Eqns. (43, 44), which is the largest for small τ and small SZA. This result is consistent with Schumann et al. [21]. Figure 15 shows the RF dependence on the ice particle habit with optical depth of the contrail. Figure 15 stresses the importance of particle habits for daytime contrail RF. Although spheres may cause a net warming even for thick contrails, the other habits may cause a net cooling of the atmosphere during the daytime for rather thin contrails because of far stronger sideward scattering causing (up to 100%) stronger RF_{SW} . Also, RF_{LW} depends on particle habit. The LW difference between spheres and rough aggregates amounts to 30%. For other habits the differences remain below 20%. All these results are consistent with Markowicz and Witek [22] and Schumann et al. [21].

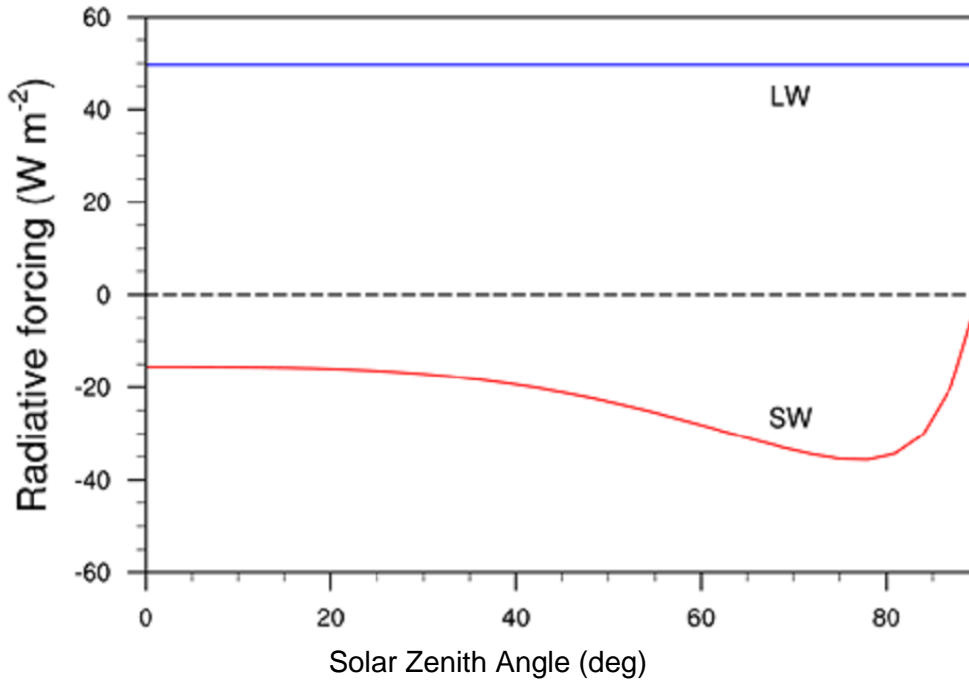


Figure 14. Longwave (LW; blue line) and Shortwave (SW; red line) Radiative Forcing (RF) as a function of Solar Zenith Angle (SZA) for sphere habits, $\tau = 0.52$, $r_{eff} = 16\mu m$, $A = 0.2$, $S_0 = 1370 W/m^2$, $T = -44.6^\circ C$, and $OLR = 279.6 W/m^2$

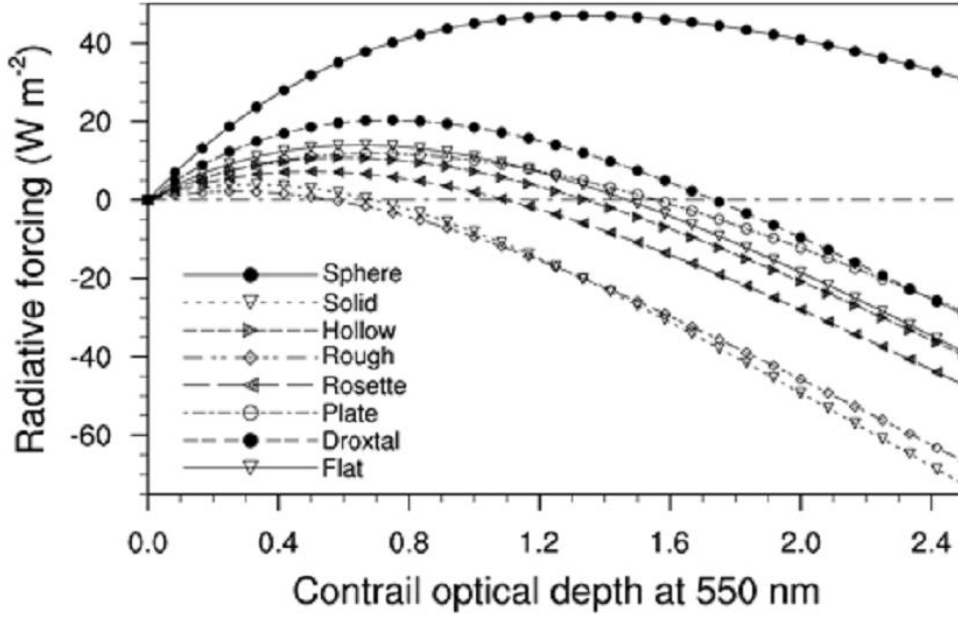


Figure 15. Net Radiative Forcing as a function of contrail optical depth (τ) at $0.55\mu\text{m}$ for various particle habits with $r_{\text{eff}} = 16\mu\text{m}$, $S_0 = 1370\text{W}/\text{m}^2$, $A = 0.2$, $\text{SZA} = 30^\circ$, $\text{OLR} = 279.6\text{W}/\text{m}^2$, $T = -44.6^\circ\text{C}$

Some comments on CoCiP's RF computation method are:

1. LW radiative forcing RF_{LW} in Eqn. (37) is constrained to positive values, where $RF_{LW} = 0$ if ambient temperature satisfies $T_C^{k_T} \geq \text{OLR}$. Similarly, SW radiative forcing RF_{SW} in Eqn. (38) is constrained to negative values, where $RF_{SW} = 0$ if and only if $A_{\text{eff}} = t_A$. The values of constant parameters such as k_T and t_A can be found in Appendix B. This ensures in the model that contrail SW radiative forcing cools the earth while contrail LW radiative forcing warms the earth.
2. Total net instantaneous radiative forcing per unit horizontal contrail coverage (RF_{net}) is a direct summation of RF_{LW} and RF_{SW} , i.e., $RF_{\text{net}} = RF_{LW} + RF_{SW}$. RF_{net} resulting from all aviation activities in the United States or globally at any given time can be computed by aggregating local contrail segments' RF_{net} weighted by their horizontal coverage areas.
3. RF_{net} at the same location changes hourly as solar zenith angle (θ or μ) changes. It is estimated that contrails normally warm the earth at night ($RF_{\text{net}} > 0$) and cool the earth during the day ($RF_{\text{net}} < 0$).
4. All constant parameters in Eqns. (37-45) are calculated using least square methods, where both inputs and outputs are from the library for radiative transfer (libRadtran) [20], [21].
5. Contrail cloud optical depth can be computed using a dynamic contrail model. The paper [20] suggests that linear and thin contrail clouds typically have an optical depth of order 0.1-0.3.

5. Radiative forcing calibration of ACSM

ACSM calculates contrail RF using methods similar to CoCiP to balance computational efficiency with reasonable fidelity. The RF computation methods of CoCiP have been validated with good performance using both numerical simulation data and some imaging satellite observation data [11], [20], [21]. In this section, RF results from ACSM are verified to be consistent with those from CoCiP under the same conditions.

ACSM was applied to the intercomparison case of Myhre [23]. This test case compares instantaneous TOA RF from various global models with state-of-the art RTMs (radiative transfer models) and realistic distributions of temperature, clouds, and surface properties, for one year (2006) of meteorological data either from an NWP (numerical weather prediction) model output or a global circulation model. This test considers a 1% homogeneous contrail cover with fixed contrail properties at 10.5km altitude and optical depth of 0.3. For simplicity, it assumes that differences in single-scattering properties of contrail particles do not influence the intercomparison. So, particles with wavelength-independent properties from Myhre were used. ACSM used NASA's Modern Era-Retrospective Reanalysis for Research and Application (MERRA) data that provide global 6-hourly 3-D pressure and temperature with $2/3 \times 1/2$ degree horizontal resolution, 3-hourly 3-D cirrus ice water content (IWC_C) with $3/2 \times 3/2$ degree horizontal resolution, and 1-hourly 2-D radiative fluxes (OLR, RSR, SDR) at TOA with $2/3 \times 1/2$ degree horizontal resolution for the year 2006. Refer to Appendix C for more detailed information on how to access the MERRA data. The optical depth of natural cirrus above a contrail is computed from these data for given cirrus-extinction $\beta_C = 3Q_{Cext}IWC_C/4\rho_{ice}r$, ice bulk density $\rho_{ice} = 917kg/m^3$, and cirrus particle extinction efficiency $Q_{Cext} = 2$ [21]. The effective radius, r , is determined as a function of temperature and ice water content in the MERRA data following the method by Sun and Rikus [24]. Figure 16 shows the global horizontal distributions of SW, LW, and net annual mean RFs, derived from ACSM using MERRA data with 1-hour interpolation. Fig. 16 shows that the maximum negative RF_{SW} is over dark surfaces (cloud-free ocean areas), whereas RF_{SW} is small over snow region like Arctic and Antarctic and high clouds near the Inter-Tropical Convergence Zone (ITCZ). The maximum RF_{LW} is computed for a contrail layer over the warm and cloud-free deserts in North Africa and Australia and in the subsiding branches of the Hadley cell over the sub-tropical oceans. For the net RF, positive values appear everywhere in this study. However, the values are close to zero over the maritime continent in the tropical western Pacific, the Himalayas, and parts of the Antarctic.

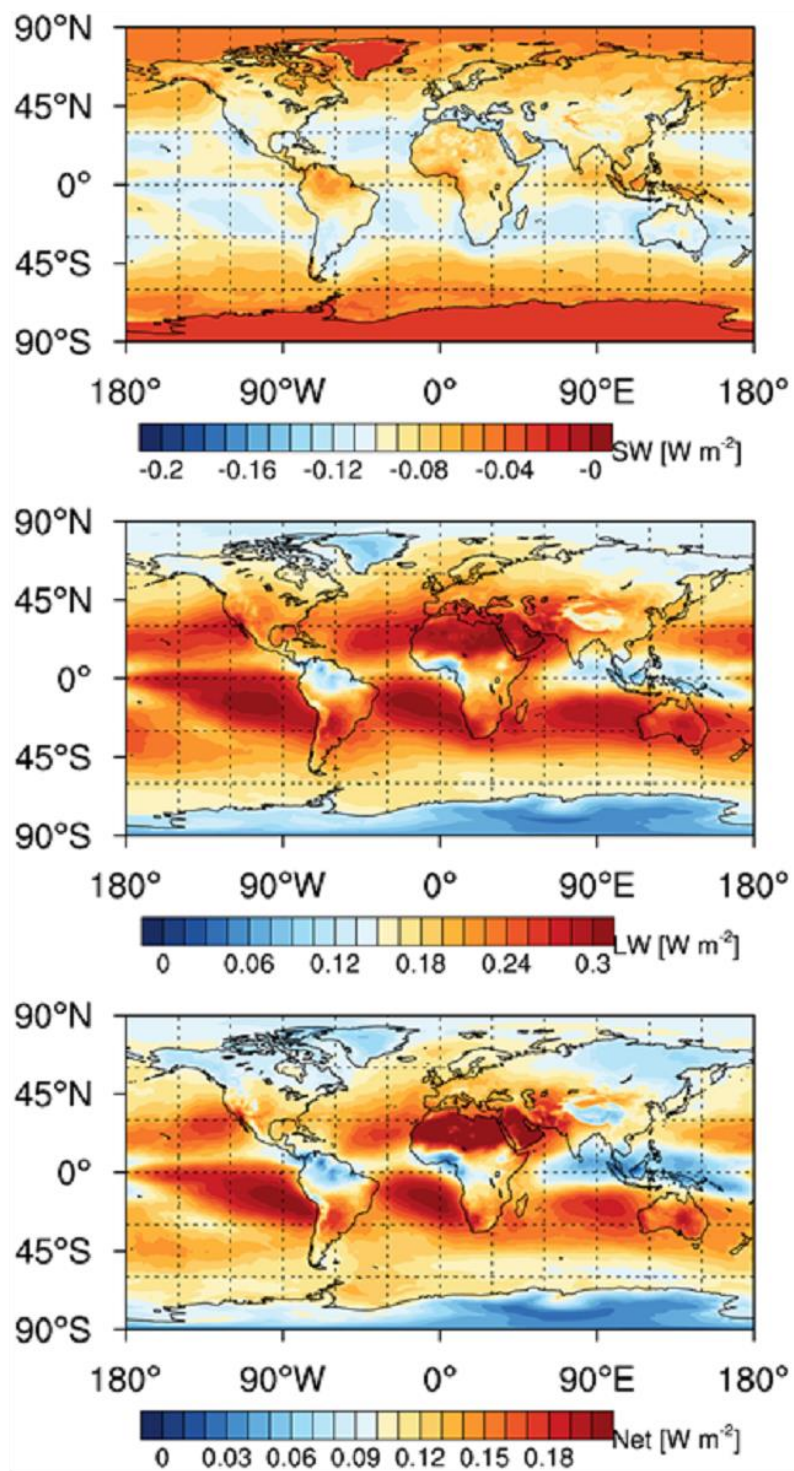


Figure 16. Global distributions of annual mean local (top) Shortwave (SW), (middle) Longwave (LW), and (bottom) net radiative forcing (RF) for globally homogeneous contrail layer with 1% cover at 10.5km altitude and particle properties from Myhre et al. [23]. From the top to bottom panels, area-weighted averages are $-0.086(\text{SW})$, $0.21(\text{LW})$, and $0.13(\text{net}) \text{ W/m}^2$

Next, area-weighted global mean values of RF forcing in Fig. 16 are -0.086 (SW), 0.21 (LW), and 0.13 (net). The SW/LW ratio in this study is 0.405, which is consistent with the range [0.21-0.55] found in previous studies [25]. The ratio deviates by less than 10% from the previous studies using similar meteorological data and RTM. According to Schumann and Graf's result, the SW/LW ratio from the diurnal actual traffic is about 20-30% larger than the RF computations based on a uniform distribution of traffic similar to this experiment. As expected from contrail RF computation equations described in the previous subsection, the ratio is dependent upon the treatment of several properties like optical depth and ice particle size and habit of the contrail, SZA, and temperature difference between the contrail and ambient atmosphere. The SW/LW RF ratio is also dependent on the radiation budget of the Earth globally and regionally. In this study, the area-averaged global mean values of the OLR, RSR, and SDR from the MERRA data in 2006 are 242.66 , 99.98 , and 341.33 W/m^2 . These values agree well with previous studies (e.g., Schumann et. al [21], [25]). Here, the area weighting is based on Gaussian weights as a function of the cosine of latitude.

The ACSM can be used to estimate the RF due to contrails resulting from actual traffic distribution instead of uniformly distributed traffic. This will provide RF due to contrails in different regions, seasons, and day and night times. The resulting contrail RF as a function of location and time can be used in designing aircraft routes that minimize the impact of aviation on climate. To assess this capability, Figure 17 shows global horizontal distribution of contrail RF_{net} for the entire 2013 in the United States and North Atlantic Flight Corridor (NAFC). The RF_{net} has a pattern similar to RF_{net} distribution using uniform traffic distribution in Fig. 16 (bottom). The US (20N-50N, 60W-130W) and NAFC (30N-75N, 10W-60W) regions are shown as green boxes in Fig.17. The diurnal contrail RF variations as a function of time in these regions are depicted in Fig. 18.

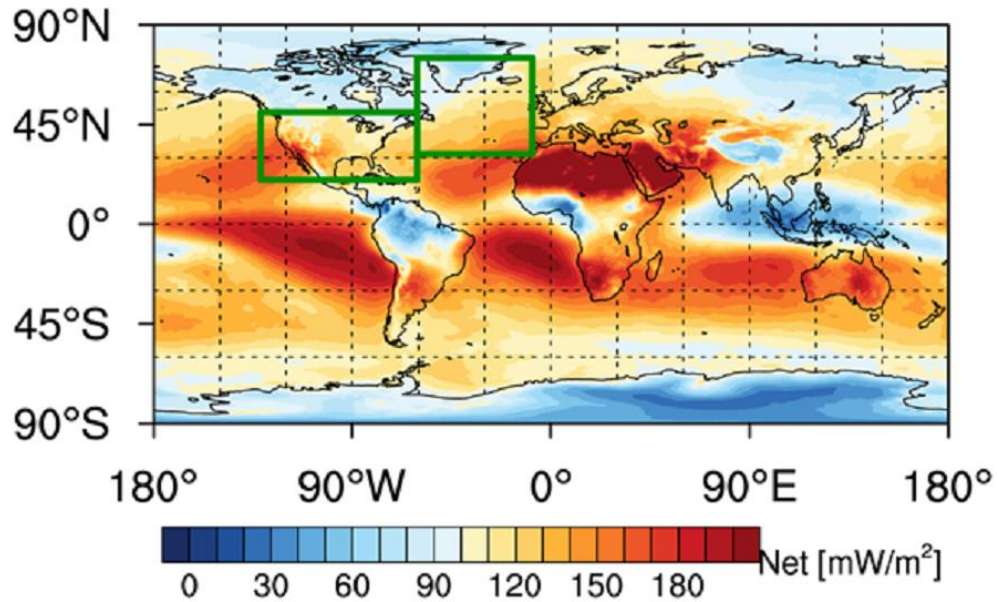


Figure 17. Global horizontal distributions of the net radiative forcing from 1% homogeneous contrail cover at 10.5km altitude and particle properties from Myhre et al. [23] for 2013. Green boxes in US (20N-50N, 60W-130W) and North Atlantic Flight Corridor (NAFC)

As expected, the warming effect due to positive contrail RF_{LW} does not significantly differ between daytime and nighttime (Fig. 18). However, cooling effect due to the negative contrail RF_{SW} is maximum during daytime, which partially cancels out the warming effect of contrail RF_{LW} (Fig. 18). Therefore, net contrail RF is the largest in the nighttime. This provides an important decision-making point of information that nighttime flights could result in a larger potential climate impact due to contrail formation than daytime flights. This pattern is almost the same in both US and NAFC areas with a shift due to different daytime intervals (Fig. 18 top and bottom). In each region, the seasonal differences of this pattern are also described in Figs. 19 and 20. In US (Fig. 19), reduction of net RF during daytime is larger in winter than in summer mainly due to the distance between the Earth and Sun. And the reduction interval is shorter in winter than in summer because of the duration of sunshine. Similar results for NAFC are shown in Fig. 20.

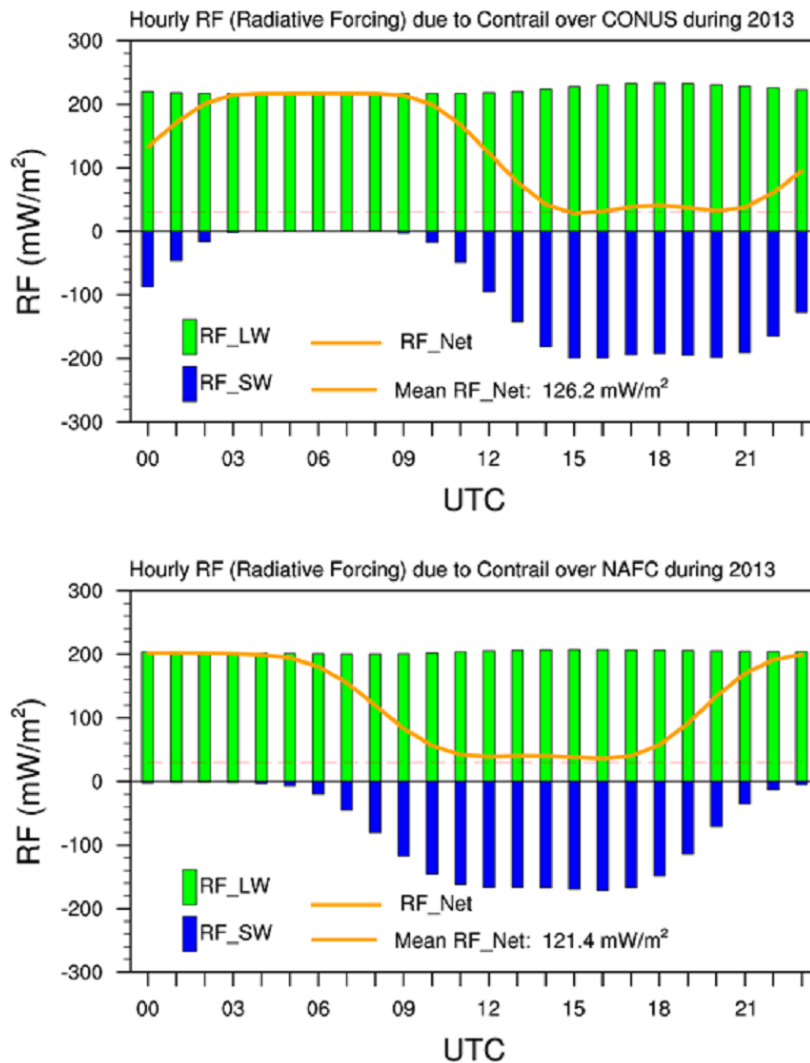


Figure 18. Diurnal distributions of the potential climate impact due to the change of LW RF (green bars), SW RF (blue bars), and net RF (orange lines) by a 1% homogeneous contrail layer at 10.5km altitude in US (top) and North Atlantic Flight Corridor (NAFC) (bottom) regions. Note that the areas for these regions are depicted as green boxes in Fig. 17.

Static value of 30mW/m^2 is also depicted as red dash lines.

This section shows results of RF by aviation-induced contrail formation in the atmosphere with static traffic distributions. Schumann's parametric methodology was adopted for the calculation of the contrail RF in specified Earth-Atmosphere conditions and with fixed contrail properties like optical depth and ice particle size and habit of the contrail. With a static traffic situation (1% homogeneous random contrail), the RF method was tested with 1-year (2006 and 2013) MERRA data that provides Earth-Atmospheric conditions with hourly temporal resolution. The contrail RF is dependent upon several factors, including the contrail properties, solar zenith angle on the contrail situation, ambient temperature at the contrail layer, radiative fluxes at TOA, and given meteorological data and given locality (spatial and temporal position of the contrail). The sensitivity tests for these factors are consistent with previous studies, which confirms that this methodology is useful for developing methods for the mitigation of the aviation-induced climate impact. The result for global mean net RF with static traffic scenario (e.g., homogeneous 1% contrail cover all over the world) was $0.13 W/m^2$, which is consistent with previous studies with the same static traffic experiments (e.g., Myhre *et al.* [23], Schumann *et al.* [21]). However, this value is somewhat different from the value ($30 mW/m^2$,) published in an IPCC report [18]. This is because the IPCC experiment is based on actual traffic data. Results of ACSM with actual air traffic is discussed in the following section. The ratio between SW and LW is also a very important indicator of model accuracy, no matter what kind of experiment is used. The ratio (SW/LW) should be in the range between 0.21 and 0.55. This is a consensus evaluation tip for the modeling of contrails. In ACSM, the ratio is 0.405 with $-0.08613 w/m^2$ (SW) and $0.2113 w/m^2$ (LW), which is within the range between 0.21 and 0.55. This implies that the modeling in ACSM is realistic and consistent with previous studies including the IPCC report. The results also show that there is a diurnal pattern to the potential climate impact from a change of RF due to the static traffic situation over both the U.S. and North Atlantic Flight Corridor (NAFC) regions in 2013.

In summary, the results from ACSM are generally consistent with those of five models shown in Myhre *et al.* [23], models in Schumann *et al.* [21] and IPCC studies [18]. As an example, Fig. 16 is similar to Fig. 11 in [21].

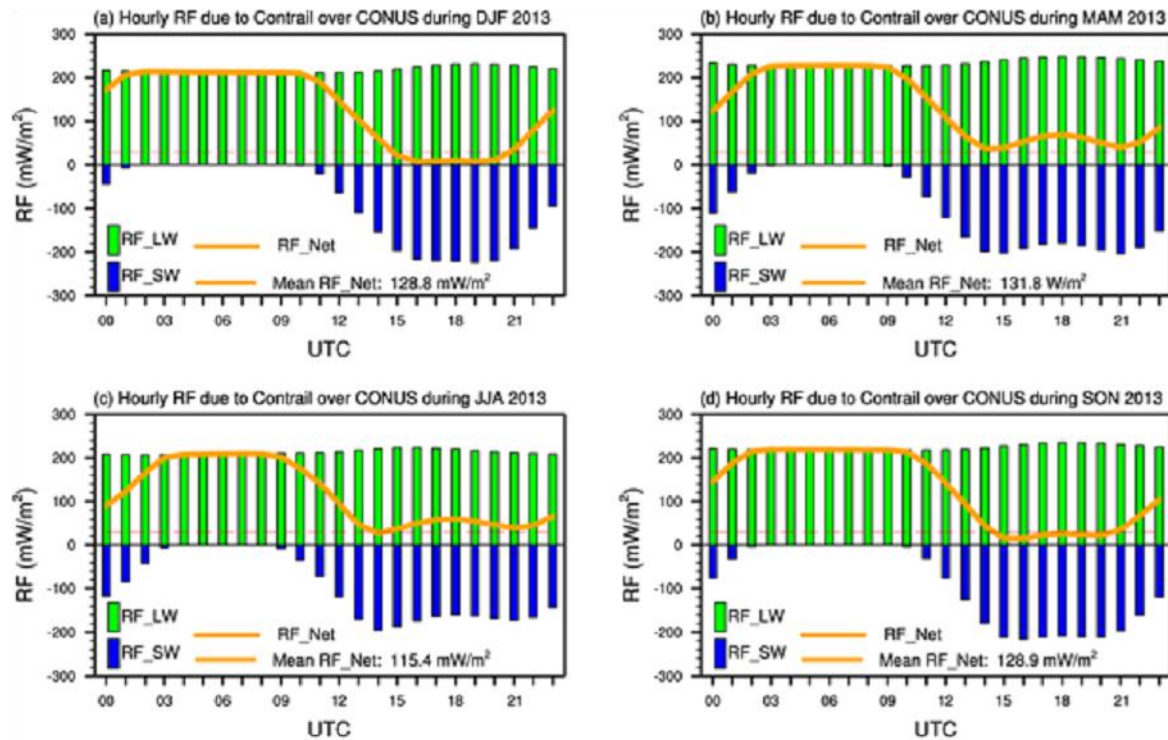


Figure 19. The same as Fig. 18 (top), Except for (a) Winter (December-February), (b) Spring (March-May), (c) Summer (June-August), and (d) Fall (September-November) in 2013.

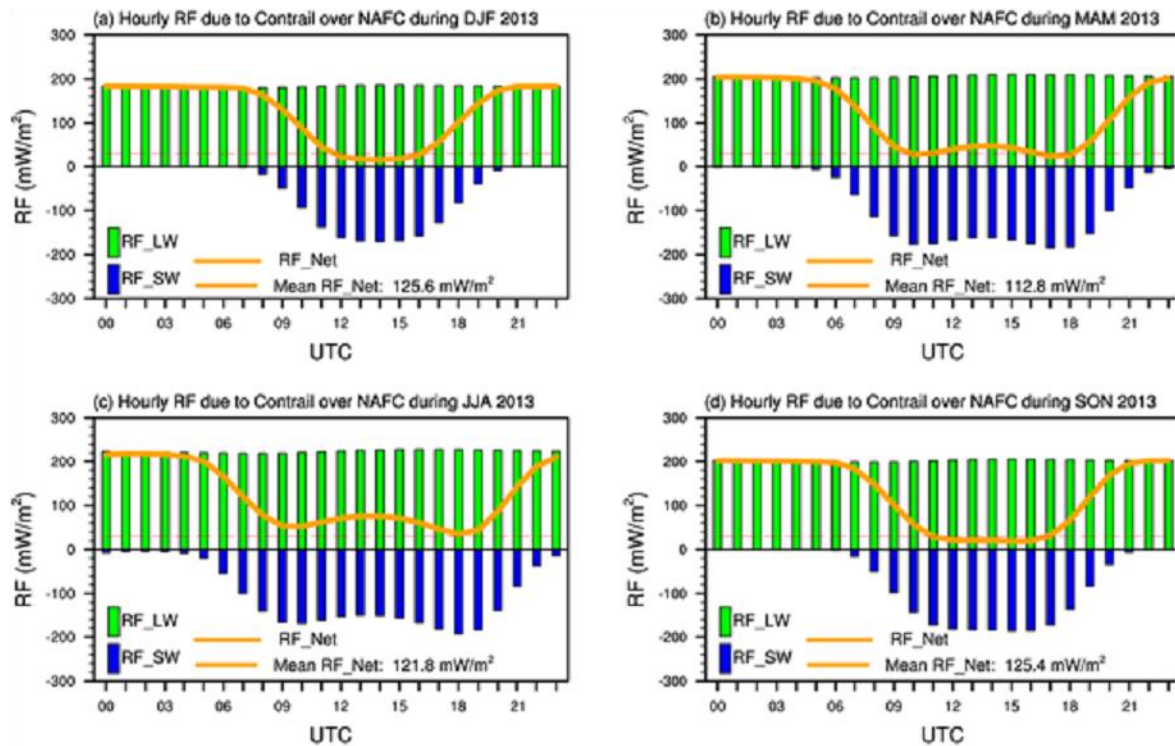


Figure 20. The same as Fig. 18 (bottom), except for (a) DJF, (b) MAM, (c) JJA, and (d) SON.

6. Case study with one-day of US air traffic

In this section, ACSM is applied to 24-hours of continental US (CONUS) air traffic. The traffic data is selected starting at 00UTC on April 23, 2010, with aircraft counts on a grid size of $13\text{km} \times 13\text{km}$ every minute. The corresponding meteorology data is downloaded from NASA's MERRA server. Figure 21 shows the net RF distribution over CONUS at different hours. From Figure 21, it is observed that most contrails occur near Georgia, Alabama, and Mississippi during early UTC hours. This trend is changed at 18UTC due to different atmospheric conditions and air-traffic density. Consequently, the net RF values are relatively higher in late evening around 7-9 PM (Eastern Day Time) than other hours. It is mainly because traffic density is the highest and the warming effect (positive RF) of longwave radiance is dominant during this period. However, during daytime (10 AM-7 PM EDT), the warming effect is partially canceled out by the cooling effect, even though traffic density is still high, which results in low RF_{net} values. Eventually, the mean RF_{net} in US on April 23, 2013, is about 50.7mW/m^2 (Fig. 22), which is consistent with estimated contrail RF_{net} suggested by the 5th assessment report of IPCC.

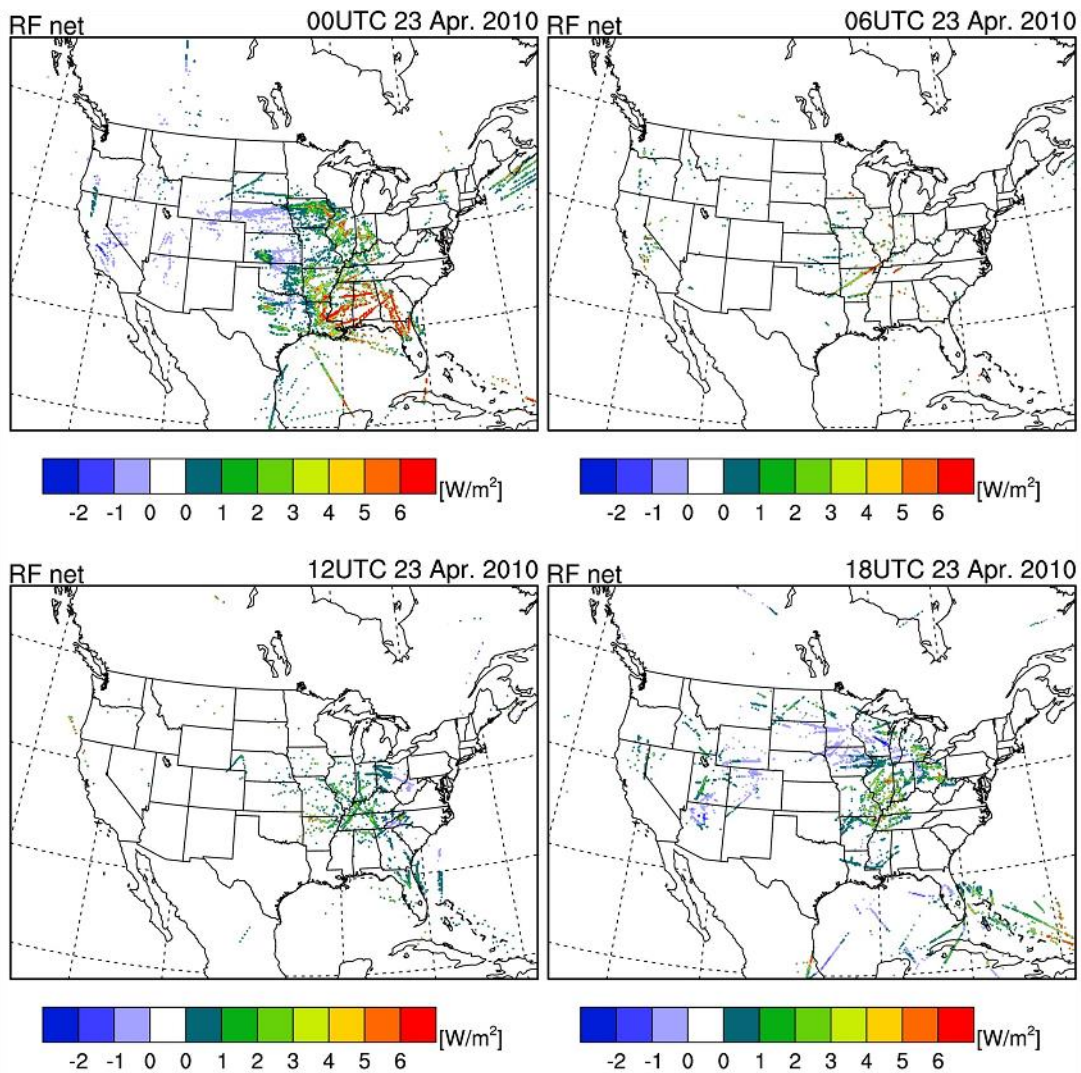


Figure 21. Horizontal distributions of the contrail-induced Radiative Forcing (RF; shading) in US at 00UTC (upper left), 06UTC (upper right), 12UTC (lower left), and 18UTC (lower right) on April 23, 2010.

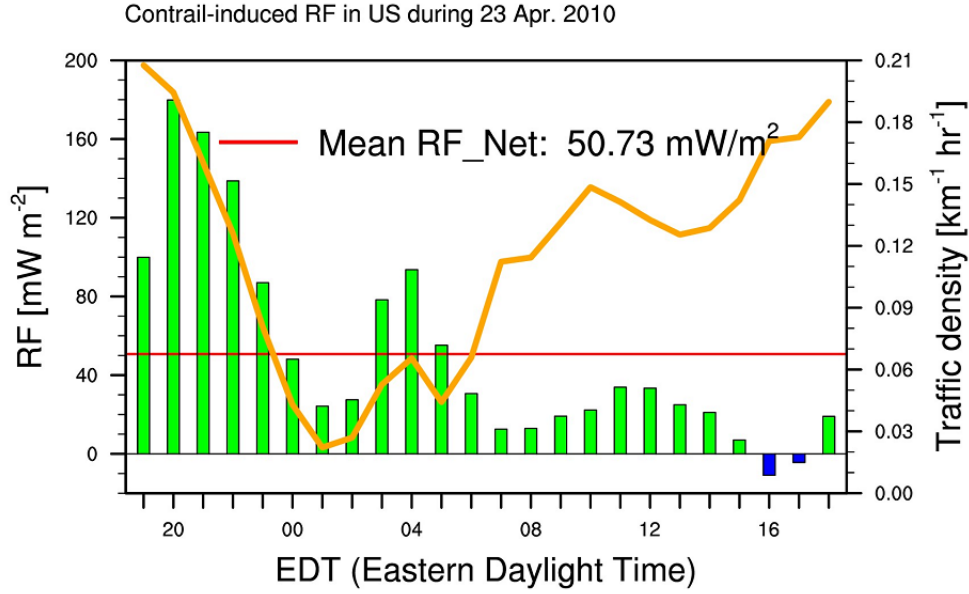


Figure 22. Hourly distributions of the contrail-induced Radiative Forcing (RF; green bars) and averaged traffic density within a given 13km×13km grid box (orange line) in CONUS on April 23, 2010.

Some final notes on the simulation are:

1. The subgrid-scale contrail properties like effective radius of the ice particle and optical depth are parametrized by a simplified methodology as a function of grid-resolved variables, as follows.

$$IWC_c = \exp(6.97 + 0.103T), \quad (46)$$

where IWC_c is ice water content of contrails with unit of mg/m^3 . Both the effective radius (r_{eff}) and optical depth (τ) of the contrails are calculated as a function of IWC_c .

2. The contrail-induced net RF is computed by the Schumann's parametric methodology, as introduced in previous sections. In this methodology, the contrail RF is regarded as a small disturbance of the net RF relative to radiative fluxes at TOA without contrail. TOA fluxes and ambient atmospheric conditions are taken from the MERRA data.
3. The accumulated contrail net RF is computed assuming that (a) contrail clouds last one hour within the grid, (b) the coverage of the contrail is triggered by the presence of air traffic and not the amount of air traffic in the grid, and (c) the contrails in different altitudes are randomly overlapped.

7. Conclusion

This report documents the physical model of an aviation-induced contrail simulation tool. The Ames Contrail Simulation Model (ACSM) simulates the full life cycle of aviation-induced contrails and calculates the associated radiative forcing with actual meteorological and air traffic data. The case study results with 24-hour U.S. air traffic show that aviation-induced contrails have an overall positive net radiative forcing. The main contributions of this work are around improving the scientific level of understanding for aviation-induced contrails, and developing models which can be practically applied to minimize the negative impacts of aviation on climate. It is well accepted by international committees such as IPCC that contrails resulting from aviation activities are one source of global warming along with carbon dioxide emission. However, the life cycle of aviation-induced contrails, from their formation to dissipation, consists of a series of complicated dynamic processes. Because of this complexity, the scientific level of understanding for aviation-induced contrails is labeled as poor by the IPCC experts. To our knowledge, ACSM is among the very few models in the world that attempts to model the full life cycle of aviation-induced contrails and calculate the associated global warming effects estimated from radiative forcing calculations that utilize air traffic and meteorological data.

Suggested next steps are as follows: First, although the results are consistent with previously published benchmark results, the model needs further validation with satellite observation data. Second, the contrail radiative forcing depends on the background radiation field, which is significantly controlled by natural cloud properties and surface properties (i.e., surface skin temperature). NASA has a well-established and published capability for estimating contrail radiative forcing that relies on observations, including clouds that affect the background radiation fields that influence the CRF (e.g., Spangenberg et al. 2013 [26], Duda et al. 2023 [27]). So, new case studies with ACSM and NASA's satellite observation tools would provide improved contrail radiative forcing prediction. Lastly, the ACSM tool was written in MATLAB and FORTRAN. Integrating the tool with air traffic simulators for fast-time and real-time aviation contrail prediction requires redesigning the software architecture and improving the code efficiency.

References

- [1] D. Lee, D. Fahey, P. Forster, P. Newton, R. Wit, L. Lim, B. Owen and R. Sausen, "Aviation and global climate change in the 21st century," *Atmospheric Environment*, vol. 43, pp. 3520-3537, 2009.
- [2] D. Lee, G. Pitari, V. Grewe, K. Gierens, J. Penner, A. Petzold, M. Prather, U. Schumann, A. Bais, T. Berntsen, D. Iachetti, L. Lim and R. Sausen, "Transport impacts on atmosphere and climate: aviation," *Atmospheric Environment*, vol. 44, pp. 4678-4734, 2010.
- [3] B. Karcher, "Formation and radiative forcing of contrail cirrus," *Nature Communication*, vol. 9, no. 1, p. 1824, 2018.
- [4] D. Lee, D. Fahey, A. Skowron, M. Allen, U. Burkhardt, Q. Chen, S. Doherty, S. Freeman, P. Forster, J. Fuglestad and A. Gettelman, "The contribution of global aviation to anthropogenic climate forcing for 2000 to 2018," *Atmospheric Environment*, vol. 244, 2021.
- [5] A. D. Naiman, S. K. Lele, J. T. Wilkerson and M. Z. Jacobson, "A low order contrail model for use with global-scale climate models," in *47th AIAA Aerospace Science Meeting*, Orlando, FL, 2009.
- [6] M. Z. Jacobson, J. T. Wilkerson, A. D. Naiman and S. K. Lele, "The effects of aircraft on climate and pollution. Part I: Numerical methods for treating the subgrid evolution of discrete size- and composition-resolved contrails from all commercial flights worldwide," vol. 230, pp. 5115-5132, 2011.
- [7] A. D. Naiman, S. K. Lele and M. Z. Jacobson, "Large Eddy simulations of persistent aircraft contrails," in *49th AIAA Aerospace Science Meeting*, Orlando, FL, 2011.
- [8] A. D. Naiman, S. K. Lele and M. Z. Jacobson, "Large Eddy Simulation of Contrail Development: Sensitivity to initial and ambient conditions over first twenty minutes," *Journal of Geophysical Research*, vol. 116, no. D21, 2011.
- [9] U. Burkhardt and B. Kärcher, "Process-based simulation of contrail cirrus in a global climate model," *Journal of Geophysical Research*, vol. 114, 2009.
- [10] U. Schumann, "A contrail cirrus prediction tool," in *International Conference on Transport, Atmosphere, and Climate*, Aachen, Maastricht, 2009.
- [11] U. Schumann, "A contrail cirrus prediction model," *International Conference on Transport, Atmosphere, and Climate*, vol. 5, pp. 543-580, 2012.
- [12] U. Schumann, "On conditions for contrail formation from aircraft exhaust," *Meteorol. Zeitschrift*, vol. 5, pp. 4-23, 1996.
- [13] U. Schumann, P. Konopka, R. Baumann, R. Busen, T. Gerz, T. Schlager, P. Schulte and H. Volkert, "Estimate of diffusion parameters of aircraft exhaust plumes near the tropopause from nitric oxide and turbulence measurements," *Journal of Geophysical Research*, vol. 100, no. D7, pp. 147-162, 1995.

- [14] K. M. Gierens, M. Monier and J. F. Gayet, "The deposition coefficient and its role for cirrus clouds," *Journal of Geophysical Research*, vol. 108, no. D2, 2003.
- [15] J. H. Seinfeld and Spyros N. Pandis, *Atmospheric chemistry and physics: from air pollution to climate change*, John Wiley and Sons, 2006.
- [16] H. R. Pruppacher and J. D. Klett, *Microphysics of clouds and precipitation*, Norwell, Mass: Kluwer Academic, 2000.
- [17] P. Foster, V. Ramaswamy, P. Artaxo, T. Berntsen, R. Betts, D. W. Fahey, J. Haywood, J. Lean, D. Lowe, G. Myhre, J. Nganga, R. Prinn, G. Raga, M. Schulz and R. V. Dorland, *Climate Change 2007: The physical Science Basis. Contribution of Working Group I to the Fourth Assessment Report of the Intergovernmental Panel on Climate Change*, Cambridge University Press, 2007.
- [18] R. Sausen, I. Isaksen, V. Grewe, D. Hauglustaine, D. S. D. Lee, G. Myhre, M. O. Kohler, G. Pitari, U. Schumann, F. Stordal and C. Zerefos, "Aviation radiative forcing in 2000: an update on IPCC (1999)," *Meteorologische Zeitschrift*, vol. 14, no. 4, pp. 555-561, 2005.
- [19] B. Sridhar, H. K. Ng and N. Chen, "Integration of linear dynamic emission and climate models with air traffic simulations," in *AIAA Guidance, Navigation, and Control Conference*, Minneapolis, MN, 2012.
- [20] U. Schumann, B. Mayer, K. Graf, H. Mannstein and R. Meerkotter, "A parametric radiative forcing model for cirrus and contrail cirrus," in *ESA Atmospheric Science Conference*, Barcelona, Spain, 2009.
- [21] U. Schumann, B. Mayer, K. Graf and H. Mannstein, "A parametric radiative forcing model for contrail cirrus," *Journal of Applied Meteorology and Climatology*, vol. 51, pp. 1391-1406, 2012.
- [22] K. M. Markowicz and M. L. Witek, "Simulations of contrail optical properties and radiative forcing for various crystal shapes," *Journal of Applied Meteorology Climatology*, vol. 50, pp. 1740-1755, 2011.
- [23] G. Myhre, "Intercomparison of radiative forcing calculations of stratospheric water vapour and contrails," *Meteor. Z.*, vol. 18, pp. 585-596, 2009.
- [24] Z. Sun and L. Rikus, "Parameterization of effective sizes of cirrus-cloud particles and its verification against observations," *Quarterly Journal of Royal Meteorology Society*, vol. 125, pp. 3037-3055, 1999.
- [25] U. Schumann and K. Graf, "Aviation-induced cirrus and radiation changes at diurnal timescales," *Journal of Geophysical Research*, vol. 118, pp. 2404-2421, 2013.
- [26] D. A. Spangenberg, P. Minnis, B. S. T., R. Palikonda, D. P. Duda and F. G. Rose, "Contrail radiative forcing over the Northern Hemisphere from 2006 Aqua MODIS data," *Geophysical Research Letters*, vol. 40, no. 3, pp. 595-600, 2013.
- [27] D. P. Duda, W. L. Smith Jr, S. Bedka, D. Spangenberg, T. Chee and P. Minnis, "Impact of COVID-19-Related Air Traffic Reductions on the Coverage and Radiative Effects of Linear Persistent Contrails

Over Conterminous United States and Surrounding Oceanic Routes," *Journal of Geophysical Research: Atmospheres*, vol. 128, no. 6, 2023.

- [28] U. Burkhardt, B. Kärcher and U. Schumann, "Global modelling of the contrail and contrail cirrus climate impact," *Bulletin of the American Meteorological Society*, vol. 91, 2012.
- [29] U. Burkhardt and B. Karcher, "Global radiative forcing from contrail cirrus," *Nature Climate Change*, vol. 1, pp. 54-58, 2011.
- [30] FAA, "Aviation environmental and energy policy statement," 2012.
- [31] H. Appleman, "The formation of exhaust contrails by jet aircraft," *Bulletin of the American Meteorological Society*, vol. 34, pp. 14-20, 1953.
- [32] A. Chlond, "Large-Eddy Simulation of Contrails," *Journal of Atmospheric Sciences*, vol. 5, pp. 796-819, 1997.

Appendixes

Appendix A. Terminologies

- Contrail fractional coverage (b): cirrus cloud coverage percentage per grid.
- Ice water mass mixing ratio (w): mass of ice-water contained in a unit mass of dry air. $w = \frac{m_{ice}}{m_{air}}$ (g/kg).
- Ice water content (IWC): amount of ice per unit volume of air (g/m^3) (or per unit air mass (g/kg)). $IWC = \rho_{ice} w_{ice} / b (g/m^3)$. It varies from 0.05-3 g/m^3 for typical clouds on average.
- Ice water mass fraction: see ice water mass mixing ratio.
- Relative humidity with respect to water (RH_w): $RH_w = \frac{e}{e_s} = \frac{w}{w_s}$, where e is vapor pressure and e_s is saturation pressure for a given temperature, and w_s saturation mixing ratio.
- Condensation: process in which water vapor transforms into water droplet at supersaturated air environment (relative humidity > 100%). This process is also known as “Homogeneous nucleation.”
- Evaporation: opposite process to condensation in which water droplet changes to vapor
- Heterogeneous nucleation: water vapor condenses into water droplet at less supersaturated environment by adding aerosols or cloud condensation nuclei (CCN). One example is that flying aircraft engines emit aerosols that facilitate contrail forming.
- Coalescence: a process of water droplet growth when it collides with other water droplets and stick together.
- Deposition (Bergeron process): a process of ice particle growth because supercooled water droplets deposit on the ice particle surfaces. Because $e_{s,water} > e > e_{s,ice}$ at below freezing ambient temperature (normally between -10 and -40°C), this creates a subsaturated environment for liquid water but a supersaturated environment for ice. This results in rapid evaporation of liquid water and rapid ice particle growth through vapor deposition.
- Sublimation: opposite to deposition, a process of ice particle contraction because water in the ice particle changes state directly to water vapor.

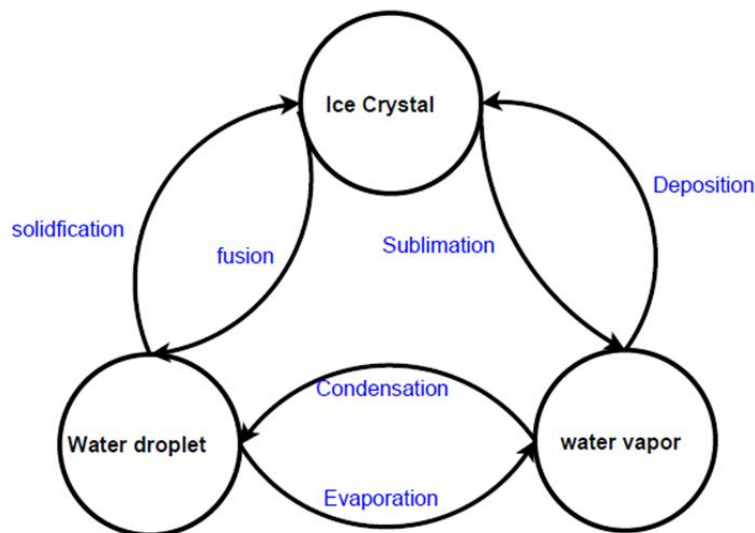


Figure 23. Cloud water component microphysical processes

Appendix B. Contrail radiative forcing parameter table

Table 3 lists the fitting parameters used to compute contrail radiative forcing in Eqns. (37)-(45) for spherical contrail ice cloud particle habit in CoCiP model [21].

Table 3: Parameters for contrail radiative forcing computation

parameter	value	parameter	value	parameter	value
T_0	152	k_T	1.935	δ_τ	0.941
δ_{lr}	0.211	δ_{lc}	0.160	t_A	0.879
Γ	0.242	γ	0.323	A_μ	0.361
B_μ	1.676	C_μ	0.709	F_r	0.512
δ_{sr}	0.150	δ_{sc}	0.157	δ'_{sc}	0.230

Appendix C. Instruction to download MERRA data

Here is an instruction for downloading the MERRA data. First of all, three types of data are required for contrail computation. Each of them has difference horizontal and temporal resolution in MERRA data: 1) 6-hourly 3-D wind, temperature, geopotential height data in pressure coordinate within $2/3 \times 1/2$ degree horizontal grid resolution, 2) 3-hourly 3-D cloud mixing ratio (mass of cloud) data in pressure coordinate within 1.5×1.5 degree horizontal grid resolution, and 3) 1-hourly 2-D total radiation flux data within $2/3 \times 1/2$ degree grid resolution. Below is for downloading these data and procedures:

1. Go to the GES DIST website (<https://disc.gsfc.nasa.gov/>).
2. In the Data Collections window, type keyword "MAI6NPANA" for 3-D wind, temp, geopotential data, type "MAI3CPASM" for 3-D cloud mixing ratio data, and type "MAT1NXRAD" for 2-D total radiation flux data.
3. Select the Date and Spatial Range.
4. Click the "Search GES-DISC".
5. Check up the check box for your data and click the "add Selected Files to Cart" tab.
6. Check up the "Subset Spatially and/or by Parameter and/or Vertical Levels..." button box.
7. Select only some variables that we will use, as follows. For 3-D wind, temp, geopotential height data, select only "u, v, and geopotential height" and select only for "500-100hPa" levels. For 2-D radiation flux data, select only "LWTUP, SWTDN, and SWTNT." For 3-D cloud mixing ratio, select only "QL, QI, and RH." Here, don't forget to check up the data format in "Netcdf" button. Then, click the "Submit selected Criteria." On the next page clicks the "Continue to Cart" and then "check out."
8. You can choose some download options depending upon your local machine. For MAC OS, download the data using "jar" file for JavaScript that is in the "More Options" tab in this page. Note that you can download using wget, curl, etc.
9. Download the Jar file, and then in your local machine please click the Jar file and choose your folder to download the data.

Appendix D. Instruction on source codes

The source codes are divided in two parts. The first part is written in MATLAB. Its outputs are contrail cloud locations given inputs of air traffic data and meteorology data. The second part is written in FORTRAN. Its outputs are instantaneous RFs given inputs of contrail cloud covers and meteorology data.

In the 1st part, input traffic data are represented as aircraft counts per minute per grid cell. Input meteorology data can be NOAA's RUC13 or RAP (covering continental U.S. and/or North America), GFS (global coverage) or NASA's MERRA (global coverage) data. The main program is ACMS_MERRA_Dec2014.m, ACMS_GFS_Dec2014.m, or ACMS_RUCRAP_Dec2014.m that read MERRA data, GFS data, or RUC13/RAP as inputs, respectively. The user can set specific year, month, and date to generate 24-hours contrail covers. The codes have been tested to work with MATLAB R2014a.

In the 2nd part, input traffic data are the same as the 1st part. However, the meteorology data can only be MERRA data because RUC13/RAP does not contain the variables required for RF computation. FORTRAN programs include two parts: 1) modules for RF_LW, RF_SW, and CONPRO, and 2) main procedure COCIP_RF_MERRA. Unix/Linux commands for running these programs are in order, as follows.

```
/home>> cd Contrail
```

Make sure there are CONTRAIL_MODULES.f90, COCIP_RF_MERRA.f90, and makefile in the directory.

```
/home/Contrail>> make
```

```
/home/Contrail>> ./COCIP_RF_MERRA
```